

ESTUARINE CO₂ GAS TRANSFER KINETICS (CORPUS CHRISTI BAY, TEXAS)

A Thesis

by

CORRIE CLARK

BS, Texas A&M University, 2013

Submitted in Partial Fulfillment of the Requirements for the Degree of

MASTER of SCIENCE

in

CHEMISTRY

Texas A&M University-Corpus Christi
Corpus Christi, Texas

May 2019

© Corrie Clark

All Rights Reserved

May 2019

ESTUARINE CO₂ GAS TRANSFER KINETICS (CORPUS CHRISTI BAY, TEXAS)

A Thesis

by

CORRIE CLARK

This thesis meets the standards for scope and quality of
Texas A&M University-Corpus Christi and is hereby approved.

Xinping Hu, PhD
Chair

Hussain Abdulla, PhD
Committee Member

Joseph D. Felix, PhD
Committee Member

May 2019

ABSTRACT

Carbon dioxide (CO₂) flux across the air-water interface at a location (27.724°N, 97.341°W) in Corpus Christi Bay, a subtropical estuary in northwestern Gulf of Mexico, was studied over the course of five weeks from November 16th to December 13th, 2018. CO₂ flux was measured using the eddy covariance technique. In addition, CO₂ concentration in both the atmosphere and sea surface was obtained. Gas transfer velocities were then mathematically derived from combination of CO₂ flux measurements and concentration differences. Gas transfer velocity was modeled as a function of wind speed.

Corpus Christi Bay was found to be a net sink of CO₂ from the atmosphere for the period of study. Average flux was -0.27 μmol m⁻² s⁻¹. Small differences in estuarine and atmospheric CO₂ concentrations (<100 ppm) were observed during the study period. Due to limited temporal data coverage, it was not possible to make long-term statements about CO₂ movement into and out of Corpus Christi Bay from this study.

Gas transfer velocity was modeled as a function of wind speed ($3.6 \text{ m s}^{-1} < U_{10} < 12.5 \text{ m s}^{-1}$), where $k_{660} = 0.36U_{10}^3$ ($R^2 = 0.64$). At wind speeds below 3.6 m s^{-1} , wind-induced turbulence contributed only 15% to gas transfer as other factors e.g., surfactant contribution and tidal motion, played a dominant role. Overall gas velocity was high (with a mean k_{660} of 146 cm hr^{-1}), with average values approximately 10 times those found in other estuarine studies. Bottom-driven turbulence caused by low water depth at the study site in addition to high average wind speeds may have caused the large gas transfer velocities.

DEDICATION

It took 1600 hours of childcare, 600 cups of coffee, 500 feet of cable, 400 hours of driving, 20 months, 2 round trips from New York, and an uncountable number of people to make this one thesis.

Special thanks to the Llanes family for their continued help with Isla, to my parents for all the support, childcare, and driving, to my granny for all the hours on the phone, to Annie for all the emotional support and the constant encouragement, and finally to Isla for all the love.

This thesis is dedicated to all of them and to everyone else who has helped me during these last two years. Not that any of them will bother to read it.

ACKNOWLEDGEMENTS

Firstly, I would like to acknowledge the help and support of my mentor, Dr. Xinping Hu. Without him, none of this would be possible. I have learned a lot in the last two years and really appreciate all the work he has put into me and this thesis.

Secondly, I would like to thank Dr. Wade McGillis. He has shown tremendous generosity in providing the technical support and equipment for this study and for his time in travelling between New York and Corpus Christi.

Thirdly, I would like to acknowledge all the other people who helped facilitate this work. The Hu Lab: Cory Saryk, Melissa McCutcheon, Larissa Dias and Hongming Yao for the technical advice, sample running, and encouragement. It was great working with you. Also thank you to everyone in the TAMUCC Chemistry Program, and to my committee for all their time and input.

Finally, I would like to thank and acknowledge the financial support from the Welch Foundation, the Texas Comprehensive Research Fund Program, and the National Science Foundation (OCE-1654232). Also, the Johnson family for the use of their pier and power supply.

TABLE OF CONTENTS

CONTENTS	PAGE
ABSTRACT.....	v
DEDICATION.....	vi
ACKNOWLEDGEMENTS.....	vii
TABLE OF CONTENTS.....	viii
LIST OF FIGURES.....	x
LIST OF TABLES.....	xii
I. INTRODUCTION.....	1
I.1 The Carbon Cycle.....	1
I.2 Air-Sea Gas Flux.....	3
I.3 Measuring Flux.....	6
I.4 Gas Transfer Velocity.....	9
II. MATERIALS, APPARATUS & PROCEDURES.....	18
III. RESULTS AND DISCUSSION.....	24
III.1 CO ₂ Flux Measured Using EC.....	24
III.2 Gas Transfer Velocity.....	30
III.3 Floating Chamber Correction.....	41
IV. RECOMMENDATIONS.....	42
V. CONCLUSIONS.....	44
V.1 CO ₂ Flux.....	44
V.2 Gas Transfer Velocity.....	44
V.3 Floating Chamber Comparison.....	45

REFERENCES	46
LIST OF APPENDICES	55
Appendix A.....	56

LIST OF FIGURES

FIGURES	PAGE
Figure 1 Annual averaged CO ₂ flux map for global oceans for the year 2000.....	3
Figure 2 Solubility of CO ₂ as a function of temperature.	6
Figure 3 Solubility of CO ₂ as a function of salinity	6
Figure 4 Google Scholar search results for <i>Eddy Covariance CO₂ Flux</i>	8
Figure 5 Temperature dependence of Schmidt number	10
Figure 6 Graphic representation of the two models for gas transfer.....	13
Figure 7 Relationships between wind speed and gas transfer velocity.....	15
Figure 8 Port Authority of Corpus Christi map of Corpus Christi Bay	18
Figure 9 Diagram of equipment setup at study site	20
Figure 10 Hourly-averaged CO ₂ flux for Corpus Christi Bay	24
Figure 11 Wind direction and wind speed	25
Figure 12 Atmospheric and sea surface CO ₂ concentration.	25
Figure 13 Sea surface CO ₂ concentration (ppm)	27
Figure 14 Yealy average flowrate for the Nueces River	29
Figure 15 Monthly average flowrate for the Nueces River.	29
Figure 16 Monthly average temperatures for the end of 2018.....	30
Figure 17 Dry mole concentrations of CO ₂ in both the atmosphere and the sea surface.	32
Figure 18 Dry mole concentrations of CO ₂ from the LiCor-7500 analyzer and NOAA buoy	32
Figure 19 Relationship between wind direction and local CO ₂ concentrations.....	32
Figure 20 Hourly-average gas transfer velocities for the entire period of deployment	33
Figure 21 Time series of CO ₂ flux and $\Delta p\text{CO}_2$	34

Figure 22 Positive hourly average of values of k_{660} vs. U_{10} for complete wind speed range	34
Figure 23 Positive values of k_{660} versus wind speed at 10 m for wind speeds below 3.6 m/s	35
Figure 24 k_{660} versus vertical water speed for wind speeds below 3.6 m/s.	36
Figure 25 Diurnal trend of wind speed and astronomical tide for Corpus Christi Bay	37
Figure 26 Relationship between k_{660} and wind speed for wind speeds above 3.6 m/s	38
Figure 27 Comparison of gas transfer models.	39
Figure 28 Comparison of model C 19 with models for k_{660} vs. wind speed for coastal regions. .	40
Figure 30 Comparison of FC and EC results versus wind speed.....	41
Figure 31 Acoustic doppler velocimeter.....	42

LIST OF TABLES

TABLES	PAGE
Table 1 Models of k based on wind speed	15
Table 2 Time periods of data collection.	19
Table 3 Selected statistics.	26
Table 4 Comparison of models for relationship between k_{660} and U_{10}	38

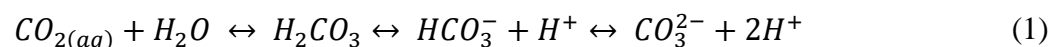
I. INTRODUCTION

I.1 The Carbon Cycle

Since the industrial revolution, anthropogenic processes that release carbon dioxide (CO₂) to the atmosphere have increased dramatically with some models predicting that the current rate of CO₂ release is the highest in the last 66 million years (Zeebe et al., 2016). These processes include deforestation, consumption of fossil fuels, and cement production (van der Werf et al., 2009). As such, atmospheric CO₂ concentration is at a high and continuing to increase, with reported atmospheric CO₂ levels over 400 ppm for the first time since the pre-industrial era (NOAA, 2018).

Excess CO₂ in the atmosphere leads to planetary warming due to the greenhouse effect (Solomon et al., 2009). Global warming could cause climatic changes including disturbances to the hydrological cycle, sea-level increases from both thermal expansion and melting ice caps, and increases in severity and frequency of extreme weather events (Easterling et al., 2000; Solomon et al., 2009). Additionally, increasing global temperatures may also slow the production rate of Northern Atlantic Deep Water, triggering extreme global cooling (Broecker et al., 1985).

CO₂ moves between the atmosphere and the ocean according to localized thermodynamic forcing. On a global scale, the oceans act as a net sink of CO₂ from the atmosphere (Takahashi et al., 1997). Approximately one third of CO₂ currently produced annually in the atmosphere is dissolved in the oceans (Gruber et al., 2019). Since pre-industrial times, the ocean has taken up a total of 48% of anthropogenic CO₂ from the atmosphere (Sabine et al., 2004). Once dissolved in the ocean, CO₂ forms part of the seawater carbonate equilibrium system. The seawater carbonate system includes the following set of equilibrium reactions:



At current ocean pH, the molar ratio between the different carbon species (CO_2 , H_2CO_3 , HCO_3^- , CO_3^{2-}) is approximately 0.5%:0.0025%:85.5%:14% (Zeebe and Wolf-Gladrow, 2001).

The net effect of CO_2 ingress into the ocean is an increase in H^+ concentration and subsequent decrease in pH (Doney et al., 2009). This phenomenon is known as ocean acidification. Since pre-industrial times, the mean pH of surface seawater has decreased by 0.1 pH unit which is equivalent to a 30% increase in $[\text{H}^+]$ (Solomon and Qin, 2013).

Ocean acidification has a negative impact on many living entities, including calcifying organisms (Doney et al., 2009; Hu et al., 2015; Riebesell et al., 2000). Calcifying organisms, for example corals, extract calcium and bicarbonate ions from the water to form calcium carbonate structures. Production of solid calcium carbonate is thermodynamically feasible if the calcium carbonate saturation state, Ω , is greater than one, where:

$$\Omega = \frac{[\text{Ca}^{2+}][\text{CO}_3^{2-}]}{K_{sp}} \quad (2)$$

K_{sp} is the solubility constant for the particular form of calcium carbonate that is being produced, either aragonite or calcite. At the current ocean pH, the introduction of CO_2 into seawater has the net effect of decreasing the concentration of carbonate ions. As $[\text{CO}_3^{2-}]$ decreases, so too does Ω and the production rate of calcite minerals (Doney et al., 2009).

Increasing CO_2 concentration, in both the atmosphere and the ocean, has a negative impact on many ecosystems (Doney et al., 2009; Rosenzweig et al., 2008). CO_2 is produced in natural and anthropogenic processes in both the atmosphere and the ocean and moves across the air-sea boundary. The direction and magnitude of CO_2 movement between these two carbon reservoirs is highly variable both temporally and spatially. Understanding and quantifying this exchange is a key component in understanding the global carbon cycle. The net movement of CO_2 between the atmosphere and the ocean is described by the air-sea flux.

I.2 Air-Sea Gas Flux

Gas movement across the air-sea boundary is dependent on two factors: the thermodynamic concentration gradient and the kinetic gas transfer velocity. The concentration gradient dictates the direction of net movement while the gas transfer velocity describes the rate of movement. The mathematical description of CO₂ flux is:

$$F = k * K_0 * (pCO_{2,water} - pCO_{2,atmosphere}) \quad (3)$$

where F is flux, pCO_2 is the partial pressure of CO₂, K_0 is the CO₂ solubility constant and k is the gas transfer velocity. Subscripts water and atmosphere refer to CO₂ concentrations in both the surface water and lower atmosphere, respectively. To account for intermolecular interactions between CO₂ molecules resulting in non-ideal behavior, partial pressure can be substituted for fugacity, f , in Equation 3; however, ΔpCO_2 and ΔfCO_2 values are almost identical (Wanninkhof, 2014). CO₂ concentration is generally reported as a dry-mole fraction (xCO_2) in units of ppm. For calculations, dry-mole fraction is converted to partial pressure (pCO_2) in units of atm by multiplying xCO_2 with dry-pressure (i.e., barometric pressure minus water vapor partial pressure).

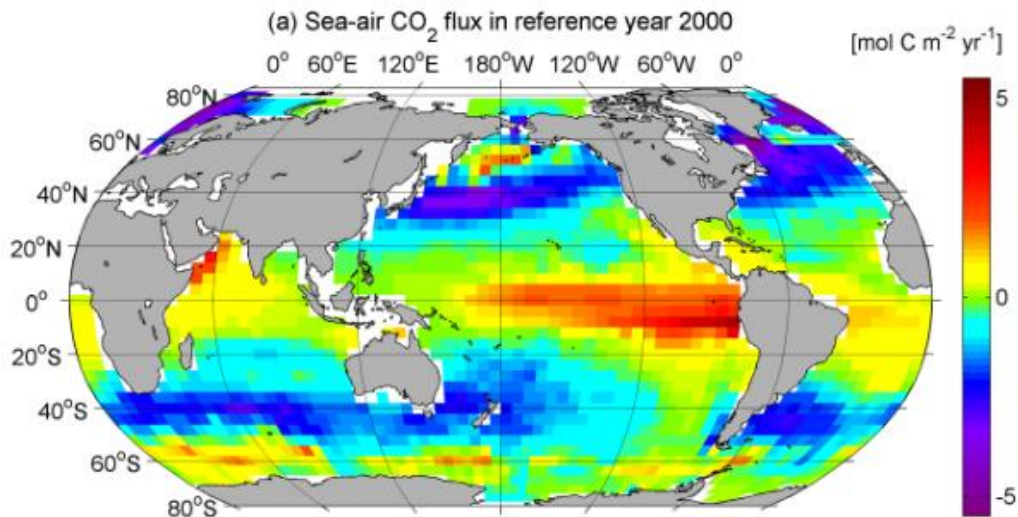


Figure 1 Annual averaged CO₂ flux map for global oceans for the year 2000. Positive flux direction is from ocean to the atmosphere <https://www.pmel.noaa.gov/co2/file/CO2+Flux+Map> (NOAA PMEL Carbon Program, 2000; Takahashi et al., 2009).

Global open ocean CO₂ fluxes are generally well documented and show distinct temporal and spatial variations (Fig. 1). By comparison, CO₂ fluxes for coastal regions are less well defined due to complex biogeochemical and physical processes and thus remain a key area of ongoing research. The Ocean Carbon and Biogeochemistry (OCB) program, which is sponsored by the National Aeronautics and Space Administration (NASA) and the National Science Foundation (NSF), lists *estuarine and coastal carbon fluxes* as one of its six future research concentrations (Benway and Doney, 2014).

Refining coastal, particularly estuarine, air-sea gas flux estimates is an important step in understanding the role oceans play in the global carbon cycle. Despite only comprising 0.2% of the surface area of the ocean, estuaries have been estimated to account for up to 10% of total global air-sea CO₂ flux (Bauer et al., 2013). Average CO₂ flux for the open ocean is $-0.6 \text{ mol m}^{-2} \text{ yr}^{-1}$ where the negative sign indicates net movement of CO₂ into the ocean (Takahashi et al., 2002). However, estuaries are considered to be, in general, a net source of CO₂ to the atmosphere (Cai and Wang, 1998; Frankignoulle et al., 1998) with fluxes as high as $440 \text{ mol m}^{-2} \text{ yr}^{-1}$, which was measured in the Scheldt Estuary, the Netherlands (Borges, 2005). In fact, European estuaries have been estimated to release between 30 to 60 million tons of carbon per year, equivalent to 5 – 10% of the total anthropogenic carbon released in Western Europe (Frankignoulle et al., 1998). Estuarine carbonate chemistry differs from that of the open ocean due mainly to effects of riverine input and anthropogenic activities (Bauer et al., 2013; Borges, 2005; Cai and Wang, 1998; Frankignoulle et al., 1996; Hu et al., 2015). High levels of nutrients from river runoff increase photosynthesis such that the rate of primary production in coastal waters is estimated to be twice that of the open ocean (Wollast, 1998). However, CO₂ consumption from estuarine primary production has been shown to be more than offset by subsequent CO₂ production from bacterial

respiration (del Giorgio et al., 1997). Other factors, such as CO₂ upwelling in shallow coastal waters and photooxidation of organic carbon, may also increase surface water $p\text{CO}_2$ (Alvarez et al., 1999). Therefore, estuarine surface waters are typically supersaturated in CO₂ resulting in a net release of carbon to atmosphere (Borges, 2005).

Supersaturation of CO₂ occurs when the concentration of CO₂ is greater than the equilibrium concentration. The equilibrium concentration of a sparingly-soluble dissolved gas (e.g., CO₂) is described by Henry's Law:

$$p_i = k_H C_i \quad (4)$$

where p_i is the partial pressure of species in the gas phase (atmosphere), C_i is the concentration of species in the liquid phase (ocean) and k_H is the Henry's Law constant, a measure of solubility, that is dependent on the gas species, temperature, pressure, and salinity.

Solubility of CO₂ in seawater is a strong function of temperature (Fig. 2). An increase in brackish water (salinity 22) surface temperature from 20 °C to 30 °C, results in a 23% decrease in CO₂ solubility (Weiss, 1974). Temperature patterns in the estuarine surface waters follow both diurnal and seasonal patterns and are also affected by cloud coverage and other weather events. Temperature-driven diurnal variations in surface $p\text{CO}_2$ have been shown to be up to 60% (Dai et al., 2009).

CO₂ solubility is also a function of salinity (Fig. 3). Estuaries connect fresh water sources with the open ocean and as such are characterized by salinity gradients. An increase in salinity from 0 to 35 results in a decrease in solubility of 14% (Weiss, 1974). Changes in CO₂ solubility will directly affect the magnitude of CO₂ flux (Equation 3).

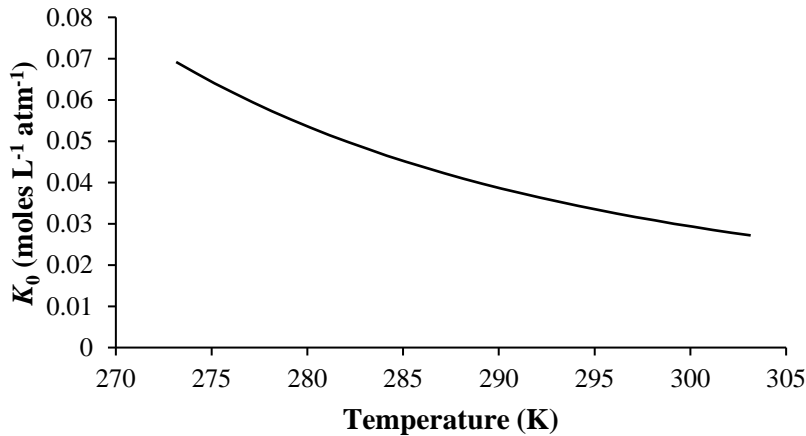


Figure 2 Solubility of CO₂ as a function of temperature at salinity of 22 (Weiss, 1974).

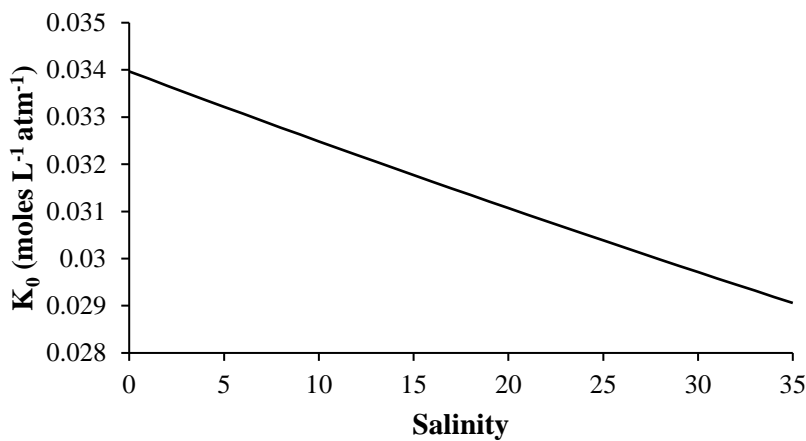


Figure 3 Solubility of CO₂ as a function of salinity at temperature of 25 °C (Weiss, 1974).

I.3 Measuring Flux

Measuring air-sea trace-gas flux directly is possible through several techniques. The most established method is through use of naturally available and deliberate gas tracers (Jähne et al., 1987; McGillis et al., 2001; Sabine, 2004). Naturally available tracers include ²²²Rn and bomb-¹⁴C (radioactive carbon isotopes released to atmosphere during extensive nuclear testing of the 1960s) and deliberate tracers include SF₆ and ³He (Wanninkhof, 2014). The tracer method involves monitoring the concentration of the selected tracer in the sea water over time to determine the rate of net movement. The rate of net movement of the trace gas can then be used to determine the flux for other trace gases by adjusting for thermodynamic properties (Clark et al., 1994). Gas tracer methods are generally not suitable for use in estuarine environments as the

tidal motion of the estuarine waters causes the tracer to be dispersed throughout the water column (Clark et al., 1994). As such, a time-averaged mass balance of the tracer concentration will then incorporate both air-sea flux and dispersion rate.

Eddy covariance is another technique used to directly measure flux. Eddy covariance is a statistical method that measures the covariance in wind speed fluctuations in the vertical direction and fluctuations in CO₂ concentration. Random fluctuations in CO₂ concentration due to the presence of turbulent eddies will average to zero over time. Therefore, any non-zero values of time-averaged CO₂ fluctuations are due to the net movement of CO₂ and not to random turbulent mixing (Burba, 2005).

Mathematically, eddy flux, F , is defined as:

$$F = \overline{\rho_a w^* s^*} \quad (5)$$

where ρ_a is air density, w^* is the fluctuation (from the mean) in wind speed, s^* is the fluctuation (from the mean) in dry mole fraction of CO₂ in air (Baldocchi, 2003). The overbar indicates that the measurements are time averaged.

The dry mole fraction, s , is calculated from the ideal gas law with atmospheric pressure corrected for the presence of water vapor to give atmospheric pressure minus water partial pressure:

$$s = q_c \frac{RT}{P(1 - x_w)} \quad (6)$$

where q_c is the molar density of CO₂ in mols per unit volume, R is the gas constant, T is the absolute temperature, P is atmospheric pressure and x_w is the mole fraction of water in the atmosphere, note that s is dimensionless (Burba, 2005).

Eddy covariance has grown in popularity since its development in the late 1980s and early 1990s. The number of publications containing the phrase “*eddy covariance CO₂ flux*” is shown in Figure 4.

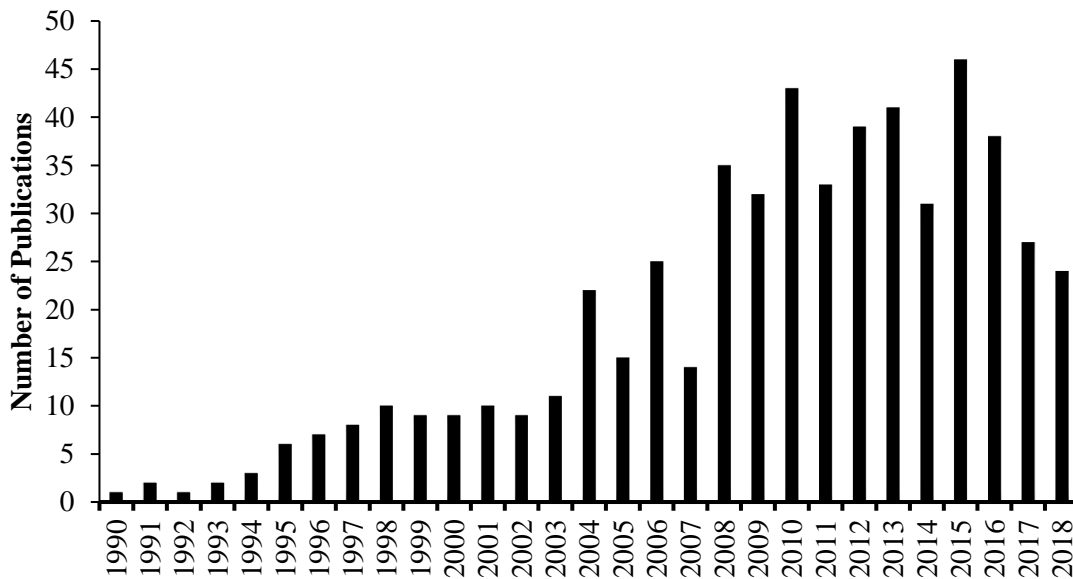


Figure 4 Google Scholar search results for “*Eddy Covariance CO₂ Flux*” on 04/11/2019.

The increasing popularity of eddy covariance is due primarily to its accuracy in a multitude of environments including coastal regions, estuaries, rivers, lakes, and the open ocean. However, eddy covariance equipment can be expensive and complicated to setup. Additionally, the equipment cannot easily be moved from site to site and requires external power and support structures.

An alternative method to measure CO₂ flux directly is to use an equilibrium chamber also known as a floating chamber. The floating chamber consists of an enclosed space that floats freely above the water surface, a CO₂ sensor is fixed inside the chamber (Martinsen et al., 2018). Initially, the headspace within the chamber has a CO₂ concentration representative of the surrounding atmosphere, once in contact with the water the CO₂ concentration within the chamber will begin

to increase or decrease as CO₂ either moves out of or into the water. The direction and rate of this initial concentration change in CO₂ is equivalent to the CO₂ flux in that area.

The floating chamber method is inexpensive and simple to use, it is also highly mobile as all equipment is contained within the chamber (Bastviken et al., 2015). However, flux measurements made with a floating chamber can be artificially high due to surface perturbations caused by the movement of the chamber on the water (Raymond and Cole, 2017). This localized turbulence will act in the same way as wind-driven turbulence to increase the gas transfer velocity. This phenomenon is more pronounced in low wind speeds as “natural” turbulence is low. It has been shown that this effect can artificially increase flux by a factor of 10 at low wind speeds (Vachon et al., 2010).

I.4 Gas Transfer Velocity

Techniques to measure CO₂ flux directly are limited in their spatial and temporal range. Therefore, common practice is to calculate flux using Equation 3 since concentrations of CO₂ in both phases can be easily measured and a gas transfer velocity can be calculated from literature (Takahashi et al., 2002; Wanninkhof et al., 2009). The gas transfer velocity, k , also called the piston velocity, is typically derived from a combination of empirical data and first principles.

A key parameter when examining gas transfer is the dimensionless Schmidt number. Mathematically, the Schmidt number, Sc , is defined as:

$$Sc = \nu/D \quad (7)$$

where ν is the kinematic viscosity (momentum diffusion coefficient) of the bulk fluid and D is the diffusivity (molecular diffusion coefficient) of the gas. The Schmidt number is important because it gives information about the magnitude of turbulent versus molecular diffusion for a particular gas under certain conditions (Jähne and Haußecker, 1998). Turbulent diffusion occurs when

parcels of fluid are physically displaced due to the presence of eddies. Molecular diffusion occurs as molecules (at temperatures above 0 K) move from areas of higher chemical potential to areas of lower chemical potential. For Schmidt numbers close to unity, both turbulent diffusion and molecular diffusion are of similar significance and solubility of the gas tends to be high in the bulk fluid (Liss and Merlivat, 1986). For large Schmidt numbers, molecular diffusion is the transport rate limiting step and solubility tends to be low (Liss and Merlivat, 1986). For example, the Schmidt number for CO₂ in air (25°C) is 0.83 and for CO₂ in seawater (20 °C) is 668 (Jähne and Haußecker, 1998; Wanninkhof, 2014). Schmidt numbers are dependent on both temperature and, to a lesser extent, salinity (Wanninkhof, 2014). For example, Figure 5 shows the relationship between Schmidt number and temperature for CO₂ at a fixed salinity of 35.

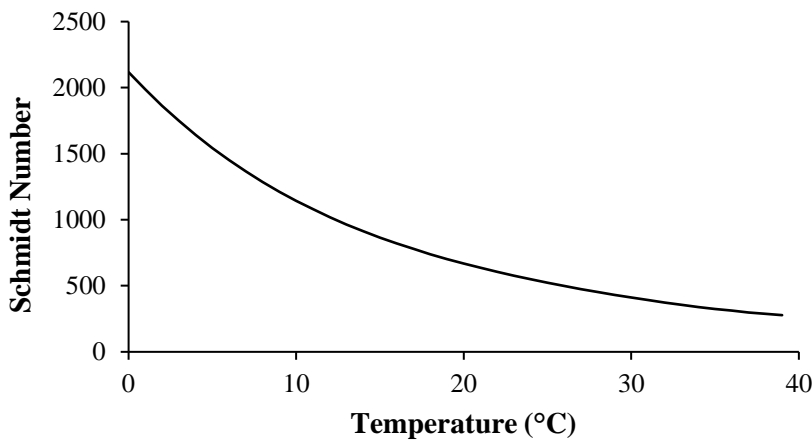


Figure 5 Temperature dependence of Schmidt number for CO₂ in seawater (salinity 35). As temperature increases, Schmidt number decreases because kinematic viscosity decreases and molecular diffusivity increases (Wanninkhof, 2014).

Schmidt numbers are also useful as they allow for the normalization of gas transfer velocities based on temperature, salinity and gas species. Gas transfer velocity models are usually reported at a Schmidt number of 660 (roughly equivalent to CO₂ in seawater at 25°C). Use of Equation 8 allows gas transfer velocity models described in literature to be adapted for use at different temperatures, salinities, and for different gas species.

$$k_x = k_{660} * \left(\frac{Sc}{660}\right)^n \quad (8)$$

where k_x is the gas transfer velocity at the Schmidt number of interest, k_{660} is the gas transfer velocity at a Schmidt number of 660, Sc is the Schmidt number of interest and n is the exponent which is dependent on the model of gas transfer being used.

There are two main models of gas transfer widely accepted in the literature (Jähne and Haußecker, 1998; Liss and Merlivat, 1986; Wanninkhof, 2014). At low wind speeds, ($<3.6 \text{ m s}^{-1}$) boundary layer models are used in which the sea surface is treated as a smooth, rigid body (Deacon, 1977; Liss and Merlivat, 1986). At higher wind speeds ($>3.6 \text{ m s}^{-1}$), surface renewal models are more suitable (Deacon, 1977; Liss and Merlivat, 1986).

In boundary layer theory for gas transfer across the air-sea interface, both the air domain and water domain have mass and viscous boundary layers that originate at the physical interface. Turbulent diffusion occurs in the viscous boundary layer, molecular diffusion occurs in the mass boundary layer (Jähne and Haußecker, 1998). Transfer of a sparingly soluble trace gas occurs via molecular diffusion at the air-sea interface. Due to high Schmidt numbers for sparingly soluble gases in seawater, water-side molecular diffusion is the rate limiting step in gas transfer (Deacon, 1977; Jähne and Haußecker, 1998; Wanninkhof, 2014). Turbulent diffusion declines at the physical boundary layer and molecular diffusion takes control; as such, the thin mass boundary layer ($\sim 100 \mu\text{m}$) on the water-side is where most of the resistance to gas transfer occurs and where the largest concentration gradient is found (Jähne and Haußecker, 1998; Wanninkhof, 2014). Therefore, in boundary layer models CO_2 air-sea gas transfer is controlled by processes occurring in the upper ($\sim 100 \mu\text{m}$ thick) layer of the water column, referred to as the sea-surface microlayer (Jähne and Haußecker, 1998; Wanninkhof, 2014; Wanninkhof et al., 2009). At wind speeds below 3.6 m s^{-1} , where the boundary layer model of gas transfer is applicable, the value of n in Equation 8 is $-2/3$ (Deacon, 1977).

At higher wind speeds ($>3.6 \text{ m s}^{-1}$), wind-induced waves ensure that the sea surface is neither smooth nor rigid. Therefore, the boundary layer model for gas transfer falls apart (Jähne and Haußecker, 1998). Instead, gas transfer is described using surface renewal models in which turbulent diffusion plays the key role (Deacon, 1977; Jähne and Haußecker, 1998). Surface renewal models depict the air-sea interface as being composed of independent parcels of fluid (eddies) which exchange with parcels of bulk fluid at a given rate (Asher and Pankow, 1991). Air-sea gas transport occurs via molecular diffusion between these parcels across the interface. Fast renewal of fluid packets at the surface with bulk fluid material maintains a maximum concentration gradient across the air-sea boundary which maximizes flux according to Equation 3 (Clayson and Curry, 1996; Jähne and Haußecker, 1998; Upstill-Goddard, 2006). Again, the greatest resistance to mass transfer is found in the liquid side so the surface renewal rate of the water becomes the rate limiting step. Surface renewal rate, λ , is defined as (Jähne and Haußecker, 1998):

$$\lambda = k/(\bar{z}) \quad (9)$$

where \bar{z} is the mean mass boundary layer thickness on the water side. At wind speeds above 3.6 m s^{-1} , where the surface renewal model of gas transfer is applicable, the value of n in Equation 6 is $-1/2$ (Deacon, 1977). A graphical representation of the two gas transfer models is shown in Figure 6.

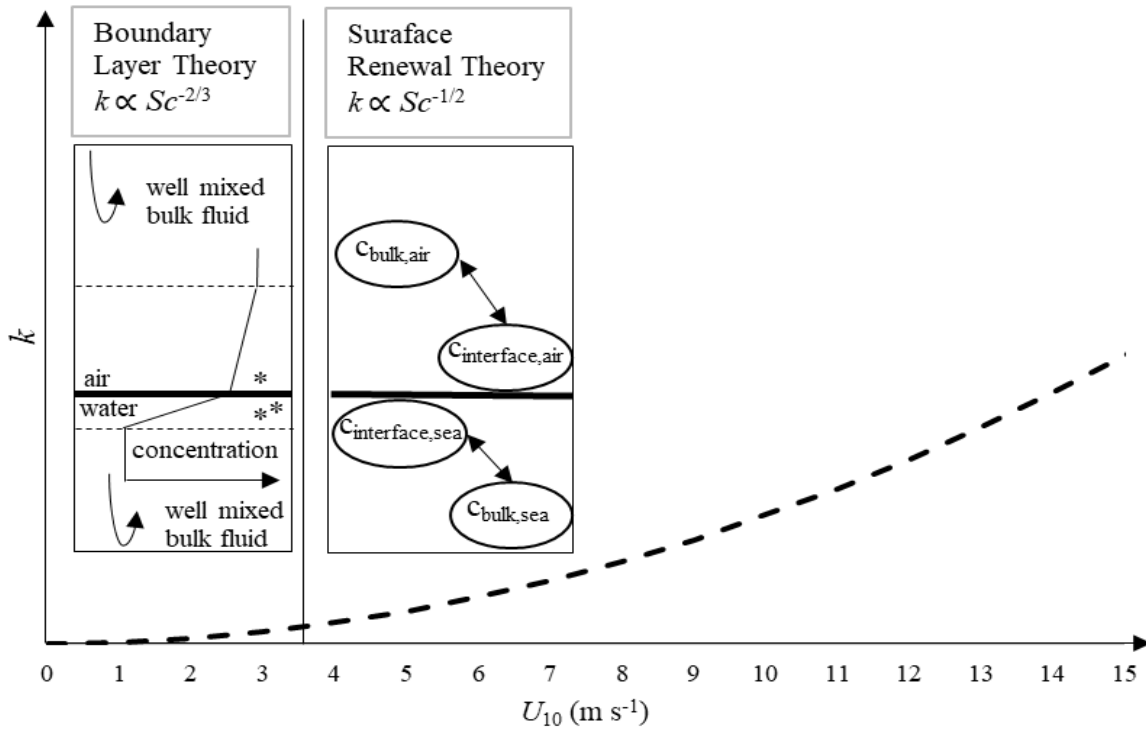


Figure 6 Graphic representation of the two models for gas transfer. Boundary layer theory is applicable at wind speeds below 3.6 m s^{-1} and surface renewal theory applies at higher wind speeds. * mass boundary layer on water-side, where most of the resistance to mass transfer occurs, ** mass and viscous boundary layers on air side which are approximately equal in thickness. Curved line represents a typical curve for the gas transfer velocity of a sparingly soluble gas as a function of wind speed.

In either model, gas transfer is enhanced by turbulent processes occurring in the sea surface microlayer (Jähne and Haußecker, 1998). Turbulent processes at the sea surface are, most frequently, caused by wind shear (McGillis et al., 2001; Wanninkhof et al., 2009; Wanninkhof, 1992). At low wind speeds, the enhancement of gas transfer is primarily due to the increase in interfacial surface area due to the presence of small wind-driven waves (Deacon, 1977; Jähne and Haußecker, 1998). However, at moderate to high wind speeds, this increase in surface area accounts for only $\sim 20\%$ of the gas transfer enhancement (Jähne and Haußecker, 1998). At moderate wind speeds, additional increase in gas transfer is thought to be due to the presence of microscale wave breaking (wave breaking without air entrainment, i.e., no whitecaps) which increases the surface renewal rate (Zappa et al., 2001). At high wind speeds, gas transfer is further

boosted by the presence of wave breaking with whitecaps and subsequent bubble formation (Wanninkhof, 1992). Bubble formation is thought to strongly enhance gas transfer as entrained gas is physically moved across the air-sea interface and, additionally, bubbles tend to cause supersaturation of the trace gas in the sea surface (Woolf, 1993).

Factors other than wind speed that are thought to affect gas transfer include rainfall, surfactant concentration, bottom-driven turbulence and biological factors (Upstill-Goddard, 2006). Rainfall and bottom-driven turbulence directly contribute to surface turbulence, enhancing gas transfer by increasing interfacial surface area and surface renewal rate (Upstill-Goddard, 2006). Whilst the presence of surfactants acts to dampen any waves, decreasing the interfacial surface area and retarding gas transfer (Wanninkhof and McGillis, 1999). Lastly, the presence of biological factors in the sea-surface microlayer can cause changes in $p\text{CO}_2$ in the upper micrometers of the water column (Dai et al., 2009).

Modelling gas transfer as a function of all the previous parameters is, in practicality, not possible. Therefore, k is usually parameterized as a function of wind speed alone, where higher wind speeds enhance gas transfer (Liss and Merlivat, 1986; McGillis et al., 2001; Wanninkhof, 2014). Wind speed increases with height above the sea surface up to a maximum value, U_{bulk} . To normalize for this, wind speed in gas transfer models is typically reported at a value of 10 m above the sea surface, denoted as U_{10} , as 10 m is ordinarily enough distance from the surface for U_{bulk} to be reached. To convert wind speed measurements taken at heights other than 10 m, the following relationship is used (Hsu et al., 1994):

$$U_{10} = U_x * \left(10/z_x\right)^{0.11} \quad (10)$$

where U_x is the measured wind speed at height z_x meters.

The most commonly used gas transfer velocity models are those developed by Wanninkhof (1992), and updated in 2014 (W14), Liss and Merlivat (1986), (LM86), and McGillis et al. (2001), (M01). These models are detailed in Table 1 and compared graphically in Figure 7.

Table 1 Models of k based on wind speed. Liss and Merlivat (1986), and Wanninkhof (2014), models state k without an explicit Schmidt number, instead the Schmidt number of interest is entered in model itself. McGillis et al (2001), is stated at a Schmidt number 660, conversion to the Schmidt number of interest is done using Equation 8.

Name	Model	Wind Speed Range
LM86	$k = 0.17\langle U_{10} \rangle (Sc/600)^{-2/3}$	$U_{10} < 3.6 \text{ ms}^{-1}$
	$k = (2.85\langle U_{10} \rangle - 9.5) * (Sc/600)^{-0.5}$	$3.6 \text{ ms}^{-1} < U_{10} < 13 \text{ ms}^{-1}$
	$k = (5.9\langle U_{10} \rangle - 49.3) * (Sc/600)^{-0.5}$	$13 \text{ ms}^{-1} < U_{10}$
W14	$k = 0.251\langle U_{10}^2 \rangle (Sc/660)^{-0.5}$	
M01	$k_{660} = 3.3 + 0.026\langle U_{10}^3 \rangle$	

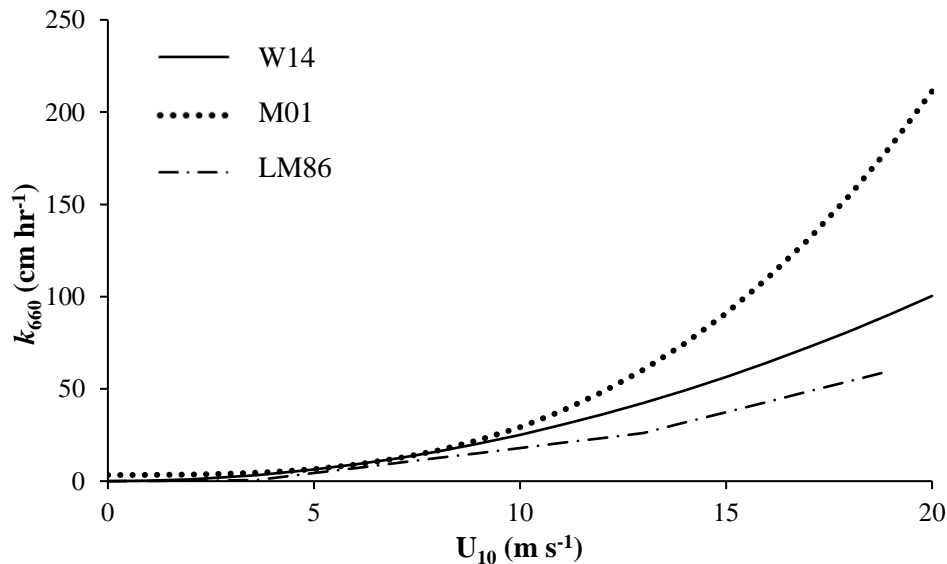


Figure 7 Relationships between wind speed and gas transfer velocity based on models by (W14) Wanninkhof (2014), (M01) McGillis et al. (2001), and (LM86) Liss and Merlivat (1986).

Although Liss and Merlivat (1986), describe a linear relationship between wind speed and gas transfer velocity, they break the function into three discrete sections corresponding to different wind speed ranges and use a different gradient for each section. This accounts for the true non-linear behavior of gas transfer as a function of wind speed and closely mimics a quadratic relationship. Wanninkhof (2014), describes a quadratic relationship between wind speed and gas

transfer velocity whilst McGillis et al. (2001), use a cubic fit. The question of a quadratic versus cubic fit for gas transfer velocity as a function of wind speed is something that has been discussed in the literature (Wanninkhof and McGillis, 1999). Early models for k were usually based on a quadratic fit with wind speed (Wanninkhof, 1992). Quadratic and cubic models agree at low to moderate wind speeds, both accounting for the decreased dependence of gas velocity at lower wind speeds where other factors, for example surfactant concentration, take a bigger role (Wanninkhof et al., 2009). However, quadratic models are found to underestimate gas velocity at high wind speeds where bubbles are thought to greatly enhance gas transfer (Woolf, 1993). Monahan and Spillane (1984), first introduced the idea that the presence of whitecaps could greatly increase gas transport, whitecap coverage has a cubic relationship with wind speed. Additionally, due to the practical difficulties in measuring gas transfer at higher wind speeds (especially from research vessels) not a lot of data exist at wind speeds $> 15 \text{ m s}^{-1}$. McGillis et al. (2001), describe the first real attempt at quantifying gas transfer at high speeds, and they determine that a cubic fit is most appropriate.

Although much work has been done on modeling gas transfer for the open ocean, comparatively little work has focused on coastal or estuarine regions (Borges, 2005). As previously discussed, gas transfer is mediated by turbulent processes in the sea-surface microlayer. For the open ocean, wind shear is by far the principal producer of turbulence in the upper water column. However, for estuarine environments, other factors are known to significantly contribute to surface turbulence (Zappa et al., 2003). Primarily, the additional contribution to surface turbulence in estuarine waters is from water shear due to tidal motion and shallow depth (Borges et al., 2004; Zappa et al., 2003). Due to the suspected importance of estuaries in the global carbon cycle, it is important that estuarine-air CO_2 exchange is well understood. However, due to the

current poor parametrization of k for estuarine waters, robustly quantifying this relationship is not possible. Additionally, current methods to measure CO₂ flux directly are either expensive and complex or potentially inaccurate. Therefore, direct measurements of CO₂ flux are not readily available.

Given the above discussion, this thesis aims to fulfil the following goals:

1. Develop a gas transfer velocity suitable for use in estuarine environments as a function of wind speed

a. Hypothesis: gas transfer in estuarine environments will be a weaker function of wind speed due to the effects of water shear

2. Describe CO₂ gas exchange for Corpus Christi Bay

a. Hypothesis: gas exchange between the atmosphere and the bay will be a strong function of wind speed, tidal patterns, temperature, light exposure, and rainfall events.

b. Hypothesis: due to high average wind speed, gas flux between Corpus Christi Bay and the atmosphere will be large

II. MATERIALS, APPARATUS & PROCEDURES

The study site for this work was a private pier located in Corpus Christi, Texas. The pier extends ~ 120 meters into Corpus Christi Bay. Corpus Christi Bay is a large (497 km²) bay with average freshwater inflow of 34 m³ s⁻¹ (Harte Research Institute, 2019). The bay is located in the northwest region of the Gulf of Mexico and is fed by the Nueces River (99% total flow) and Oso Creek (1% total flow) (Orlando et al., 1993). The bay is largely isolated from the Gulf of Mexico by a series of barrier islands. Outfall to the Gulf of Mexico occurs via Aransas Pass. Due to the semiarid nature of the region and the slow exchange of water between the Gulf and the Bay, salinity in the bay can reach values in excess of 40 (Ritter and Montagna, 1999). Average salinity for the summer months is 30 and for winter months is around 17 (Orlando et al., 1993). The bay is shallow, with an average depth of just 2 m and a maximum depth of 14 m in the dredged ship channel (Orlando et al., 1993).

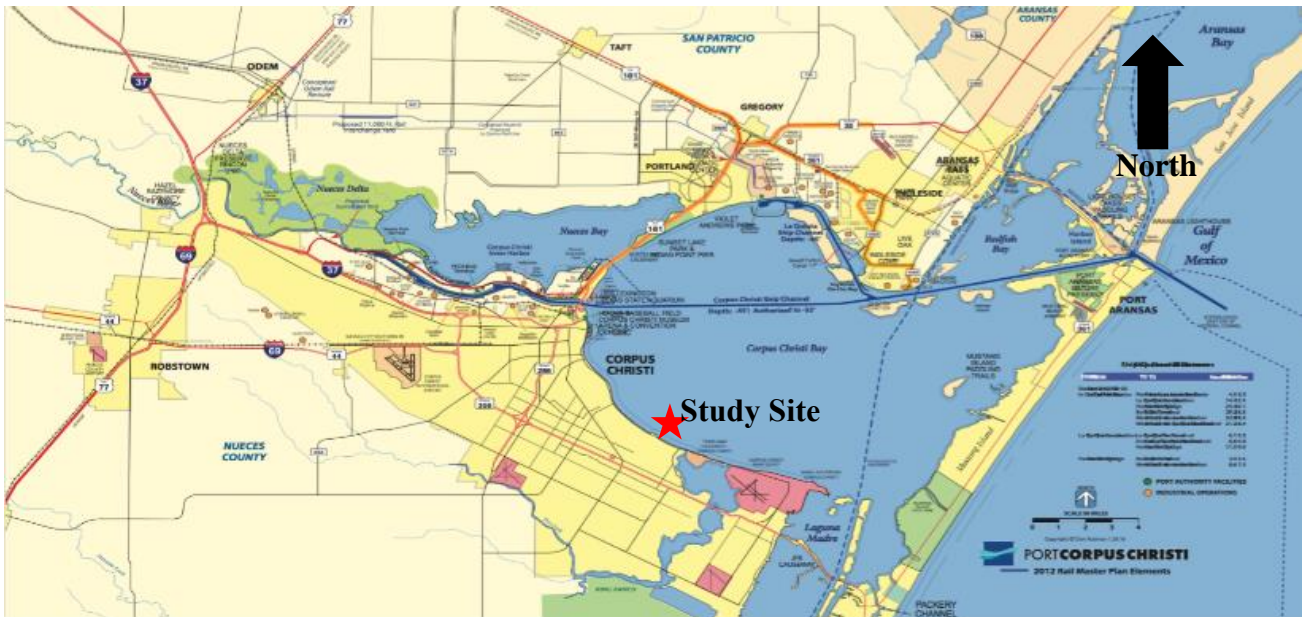


Figure 8 Port Authority of Corpus Christi map of Corpus Christi Bay showing the study site (Port Authority of Corpus Christi, 2012).

Eddy covariance method

Measurements of three-dimensional wind speed, CO₂ concentration in the atmosphere and surface water, water temperature, atmospheric temperature, pressure, and relative humidity were taken at intervals over the period from November 16th, 2018 at 23:30 (UTC) to December 13th, 2018 at 23:45 (UTC) (see Fig. 9 for the experimental setup). The intention was to take continuous samples for the entire period of deployment; however, alternating-current power from an electrical outlet located outside the pier owner's house was lost several times due to a continually tripping breaker before becoming permanently unavailable. The decision was made to switch to a gas-powered generator which was at the end of the pier, downwind from equipment to avoid interference of combustion products with CO₂ measurements. The generator had to be manually turned on for periods of data collection until the gasoline ran out after 2-6 hours. Therefore, measurements were essentially taken at discrete intervals for the rest of the sampling period. Table 2 shows each individual time periods where data were collected.

Table 2 Time periods of data collection. All times are UTC.

Period Number	Collection Started	Collection Ended
1	11/16/2018 23:30	11/19/2018 3:00
2	11/30/2018 21:30	12/3/2018 11:30
3	12/4/2018 20:00	12/4/2018 22:45
4	12/5/2018 16:30	12/5/2018 21:15
5	12/6/2018 16:15	12/6/2018 21:45
6	12/10/2018 17:45	12/10/2018 23:30
7	12/12/2018 17:45	12/12/2018 23:00
8	12/13/2018 20:00	12/13/2018 23:45

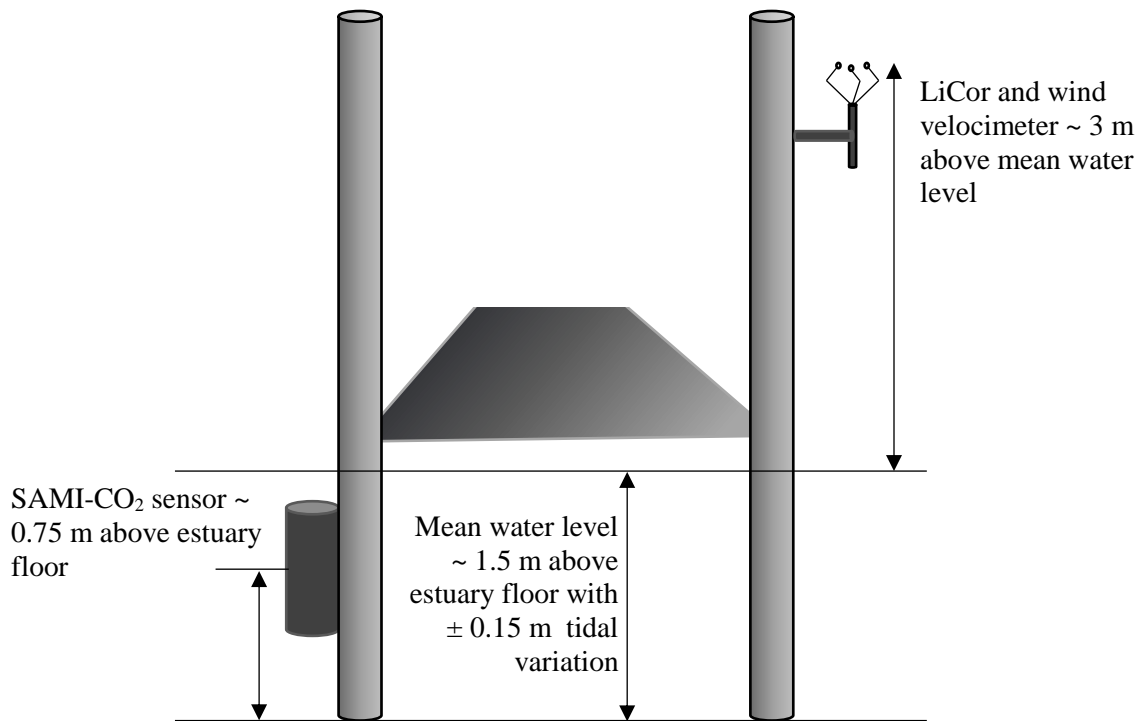


Figure 9 Diagram (not to scale) showing the relative setup of all the equipment during the data collection period.

Wind speed measurements were taken at 20 Hz frequency using an onboard sonic anemometer located in the LiCor-7500 CO₂/H₂O analyzer, manufactured by LiCOR and specifically designed for open path eddy covariance flux measurements. Calculated U_{10} values were based on the vector addition of the two horizontal components of velocity and ignored the vertical component. The anemometer read wind speeds at a height of 3 m above the sea surface. Air temperature was measured using the LiCor-7500 CO₂/H₂O analyzer.

The study site already housed a weather station operated by WeatherFlow[®] that provided meteorological data to this study. This weather station monitors barometric pressure, wind speed, and wind direction and logs averages at 15-minute intervals. The equipment is located 4 m from the sea surface. Information from this weather station was used to determine the wind direction and as an independent check for the wind speed recorded by the LiCor-7500 anemometer.

Atmospheric $x\text{CO}_2$ concentration was measured using the LiCor-7500 $\text{CO}_2/\text{H}_2\text{O}$ analyzer, manufactured by LiCOR. Readings were taken at 20 Hz. The analyzer uses infrared absorption to measure the concentration of CO_2 and H_2O in the atmosphere. Dry- CO_2 concentration is then calculated by subtracting the measured concentration of water. For CO_2 analysis, manufacturer reports a typical RMS noise value of 0.16 ppm at 20 Hz, with a typical drift of $0.1 \text{ ppm } ^\circ\text{C}^{-1}$.

The $p\text{CO}_2$ in the water column was measured using a calibrated SAMI- CO_2 sensor manufactured by Sunburst Sensors. Measurements were taken at 30-minute intervals with a manufacturer stated response time of ~ 5 minutes. The SAMI- CO_2 sensor uses a colorimetric reagent method to determine the concentration of CO_2 in the gas phase in equilibrium with the sea water. Stated accuracy is $\pm 3 \text{ } \mu\text{atm}$, precision is $< 1 \text{ } \mu\text{atm}$ and long-term drift is reported to be $< 1 \text{ } \mu\text{atm}/6$ months. Temperature was also measured with the SAMI- CO_2 sensor at intervals of 30 minutes. Manufacturer reported accuracy for the thermistor is $\pm 0.1^\circ\text{C}$ with a precision of $\pm 0.01^\circ\text{C}$.

Floating chamber measurements

The design for this chamber was adapted from Duc et al. (2013), using a SenseAir K33 ELG 10,000 ppm CO_2 sensor with onboard temperature and relative humidity sensors and an internal data logger. During operation, air was pumped from inside the chamber using a 6 V, 2 L min^{-1} compressor/vacuum pump manufactured by Thomas® (model G6/01-K-LCL) through a syringe containing magnesium sulfate that removes water vapor. The dry air was then pumped into a separate container within the chamber where the sensor is housed. Both the sensor and pump were powered by internal batteries. The dry- CO_2 mole fraction was then recorded in ppm. Flux was then calculated using Equation 11.

$$F = \frac{\Delta CPV}{RTA\Delta t} \quad (11)$$

where ΔC is the change in concentration in ppm, P is the pressure of the system (minus water vapor partial pressure), V is the volume of the chamber, R is the gas constant, T is the absolute temperature of the headspace, A is the surface area available for gas transfer and Δt is the given time period corresponding to ΔC . The initial rate of change in concentration of CO_2 within the chamber is representative of the CO_2 flux for the area.

Discrete water collection and analysis

Discrete samples of sea water for carbonate system and salinity analysis were taken at two separate times on 11/07/2018 at 9 PM (UTC) and 11/21/2018 4 PM (UTC). Continual sampling of salinity for the period of study was attempted. However, an error with the equipment meant that no salinity data were recorded. Therefore, for calculations that require salinity (e.g., Schmidt number and water vapor partial pressure) the single salinity value obtained from the sample taken on 11/21/2018 was used. Salinity throughout the period of study is not likely to have been constant. However, even a hypothetical error in salinity of 35 would only affect Schmidt number calculation by ~ 10%, water vapor calculation by ~ 2%, and overall k_{660} normalization by ~5%.

Discrete water samples were taken to analyze salinity and characterize the carbonate system for $p\text{CO}_2$ calculation. Water samples were collected within 100 m of the sampling site using the technique detailed by Dickson et al. (2007).

DIC was measured using an Apollo SciTech[®] AS-C3 DIC analyzer with onboard LiCor, Li-7000 $\text{CO}_2/\text{H}_2\text{O}$ detector. 0.5 mL water samples are reacted with a 10 mol% H_3PO_4 /10 mol% NaCl aqueous solution to release all dissolved inorganic carbon as CO_2 .

Salinity was measured using a benchtop Orion Star™ A212 conductivity meter, manufactured by Thermo Scientific™. Instrument was calibrated prior to use with control reference material of salinity 33.64 and deionized water with a salinity of zero.

pH (on a total scale) was measured using a Orion™ Ross™ electrode using the spectrophotometric method detailed in Carter et al. (2013). Measurements were made at a constant temperature of 25 °C with purified m-cresol purple as the indicator dye. The dye can itself alter the pH of the sample, to correct for this the method by Clayton and Byrne (1993), was used.

$p\text{CO}_2$ for discrete water samples was calculated using the CO2SYS software (Lewis and Wallace, 1998) with inputs of temperature, salinity, DIC, and pH. Within the software, K_1 and K_2 (carbonic acid dissociation constants) were selected from Millero (2010), and the bisulfate dissociation constant was taken from Dickson (1990).

III. RESULTS AND DISCUSSION

III.1 CO₂ Flux Measured Using EC

CO₂ flux was calculated from atmospheric water (H₂O) and CO₂ concentrations, air temperature, and atmospheric pressure data obtained from the LiCor-7500. These data were analyzed using a MATLAB algorithm developed Dr. Wade McGillis of Columbia University, which estimates scalar fluxes using the eddy covariance technique.

For the purposes of this study, measurements of wind speed, H₂O and CO₂ concentration, air temperature, and atmospheric pressure were taken at a rate of 20 Hz, and Equation 9 was time-averaged to 15-minute periods in the MATLAB algorithm. For data analysis, the reported fluxes were further bin-averaged to hourly periods to mitigate against the effect of outliers. The entire hourly-average CO₂ flux for the complete period of collection is shown in Figure 10 with each numbered section referring to a date range shown in Table 2.

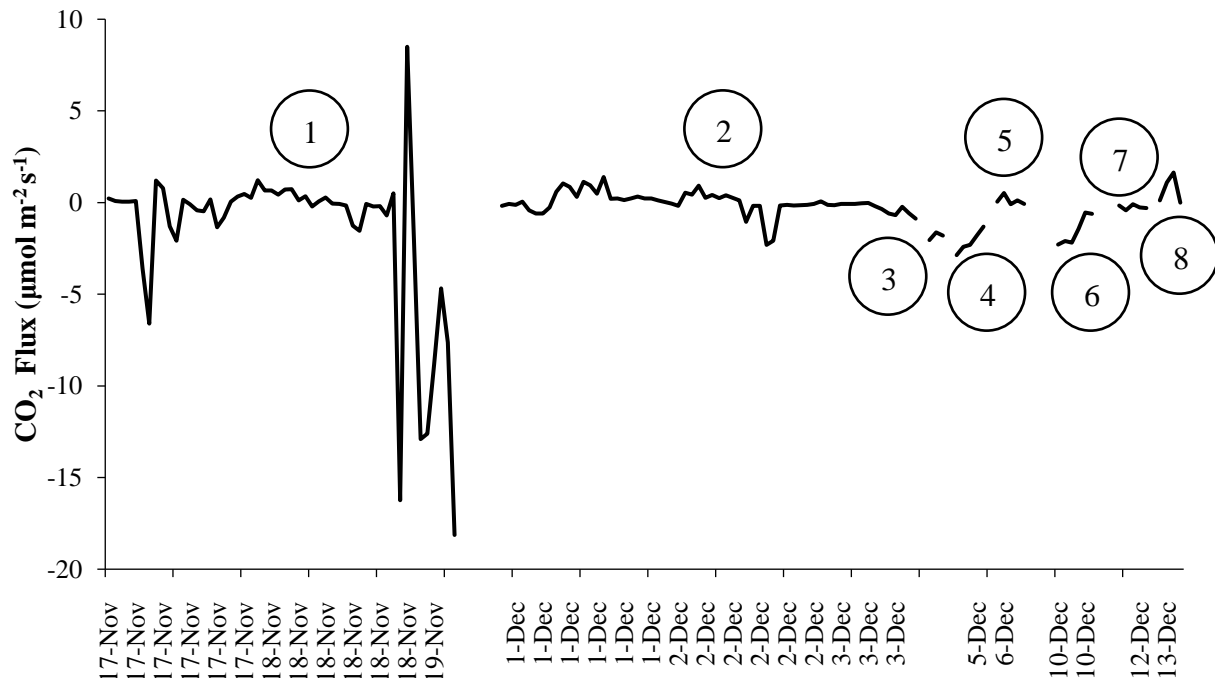


Figure 10 Hourly-averaged CO₂ flux for Corpus Christi Bay study site for all time periods that data were collected. Number beside individual trends correspond to time periods detailed in Table 2.

The average CO₂ flux for the period was $-0.777 \mu\text{mol m}^{-2} \text{s}^{-1}$, the largest CO₂ flux was observed on November 19th, 2018 at 3 AM with a value of $-18.13 \mu\text{mol m}^{-2} \text{s}^{-1}$. However, average flux is highly skewed by data from the period 7 PM November 18th, 2018 to 3 AM November 19th, 2018 as shown in Figure 10 at the end of period 1. All data collected during this period showed signs of instability, and data collection from the LiCor-7500 stopped at 3 AM November 19th, 2018 due to power loss from a tripped breaker. In addition to erratic readings from the LiCor-7500, the independent weather station and the SAMI-CO₂ sensor both showed rapid change in output during this period (Fig. 11 & 12).

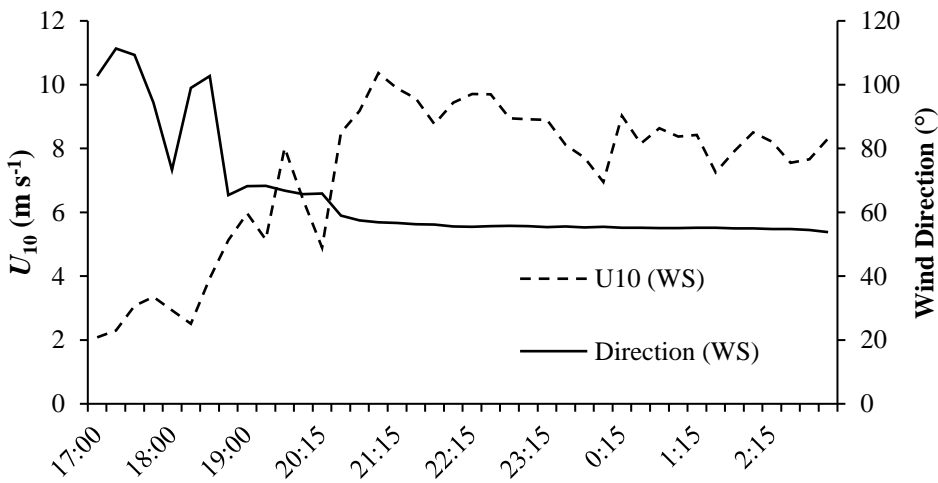


Figure 11 Wind direction and wind speed as measured by the weather station (WS) for the period 11/18/2018 5 PM to 11/19/2018 3 AM.

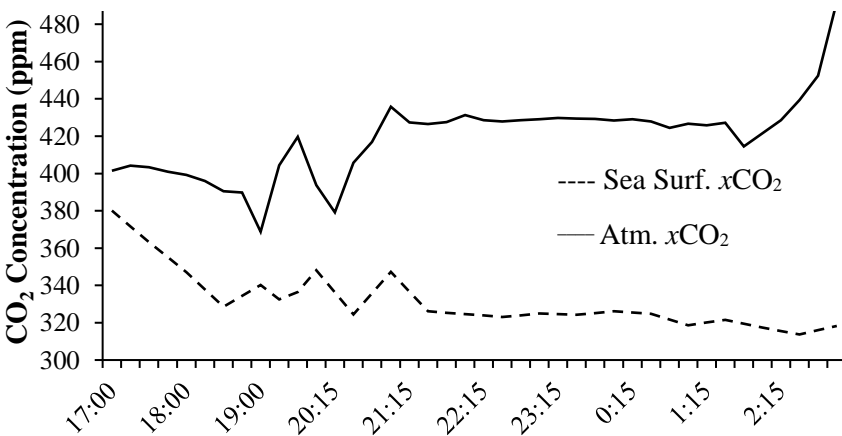


Figure 12 Atmospheric and sea surface CO₂ concentration for the period 11/18/2018 5 PM to 11/19/2018 3 AM as measured by the LiCor-7500 SAMI-CO₂, respectively.

It appears that during this period, a rapid increase in wind speed and change in direction from southeasterly winds to northeasterly winds (Fig. 11) caused an increase in atmospheric CO₂ concentration and flux (Fig. 10 & 12). One of the limitations of the eddy covariance method is that it requires stable conditions for accuracy (Burba, 2005). It is likely that the strong winds and rapidly changing wind direction during this period led to errors in the calculated CO₂ flux due to atmospheric instability. Therefore, Table 3 reports flux information for the entire period both including (entire data set) and excluding (stable subset) the data from 11/18/2018 5 PM to 11/19/2018 3 AM.

Table 3 Selected statistics from complete data set and data set excluding period 11/18/18 7 PM to 11/19/18 3 AM.

	Entire Data Set	Data Subset
Average CO₂ Flux (μmol C m⁻² s⁻¹)	-0.777	-0.270
Largest CO₂ Flux (μmol C m⁻² s⁻¹)	-18.13	-6.01
Standard Deviation	±2.94	±1.05

Regardless of whether the period of high flux is included, the net movement of CO₂ during the data collection period is from the atmosphere to the sea surface. This is in contrast with typical estuaries where net CO₂ movement is from the water to the atmosphere (Borges, 2005; Cai and Wang, 1998; Frankignoulle et al., 1998). Net positive flux from estuarine surface waters to the atmosphere is due to supersaturation of CO₂ in the upper layers of the water column, typically due to microbial respiration (del Giorgio et al., 1997). CO₂ concentration in the upper water column from the study site during the period of data collection was generally below saturation level, resulting in a negative $\Delta p\text{CO}_2$ value.

Diurnal variations in surface $p\text{CO}_2$ measurements are caused by changes in solubility due to temperature variations and to biological factors e.g. photosynthesis vs. respiration (Dai et al., 2009). To determine the relative importance of these factors, a technique developed by Takahashi

et al. (2002), was used. To calculate the ratio of thermal (T) to biological (B) factors affecting the changes in surface pCO_2 , the following equation was used:

$$\frac{T}{B} = \frac{MAX(pCO_{2,obs} * e^{\delta(T_{mean}-T_{obs})}) - MIN(pCO_{2,obs} * e^{\delta(T_{mean}-T_{obs})})}{MAX(pCO_{2,mean} * e^{\delta(T_{obs}-T_{mean})}) - MIN(pCO_{2,mean} * e^{\delta(T_{obs}-T_{mean})})} \quad (12)$$

where $pCO_{2,obs}$ and T_{obs} are the measured sea surface pCO_2 and temperature, respectively and $pCO_{2,mean}$ and T_{mean} are the mean sea surface pCO_2 and temperature (323.3 μatm and 16.5 $^{\circ}C$), respectively. σ is defined as $\delta \ln pCO_2 / \delta T$ which was calculated as 0.039 $^{\circ}C^{-1}$ for the period. T/B for the period was calculated at 0.31, indicating that non-thermal contributions to diurnal variations in sea surface pCO_2 were three times more important than thermal contributions. The diurnal pattern of sea surface CO_2 concentration for a typical period during the data collection is shown in Figure 13. Note that times are local (UTC -6 hours). CO_2 concentration in the surface water generally reaches a maximum in the early morning and a minimum in the late evening.

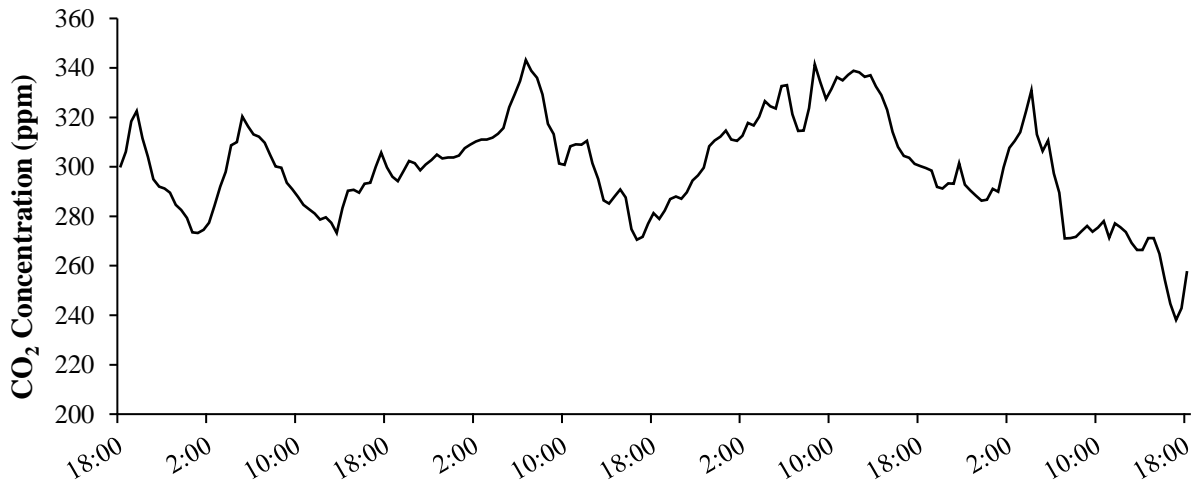


Figure 13 Sea surface CO_2 concentration (ppm) for the period 11/30/2018 to 12/4/2018. Diurnal trend is typical for entire period of collection. Times are listed as local (UTC -6 hours).

There is only one other peer-reviewed study that has examined estuarine CO_2 flux in the region. This study by Yao and Hu (2017), determined CO_2 flux from information on wind speed and xCO_2 for the Mission-Aransas Estuary (MAE) which is connected to the north of Corpus

Christi Bay. The study found that average MAE surface $x\text{CO}_2$ was 477 ± 94 ppm and 529 ± 251 ppm for a period of drought (05/2014 to 02/2015) and high rainfall (02/2015 to 04/2015), respectively. Higher CO_2 concentration in the surface water compared to the atmosphere led to the calculation of a net positive flux to the atmosphere. This is in contrast to the measured flux of this study which was net negative. However, Yao and Hu (2017), also found during the winter months (11/2014 – 02/2015) that MAE was a net sink of CO_2 from the atmosphere ($-0.10 \mu\text{mol C m}^{-2} \text{ s}^{-1}$).

Without longer term data trends on surface water $p\text{CO}_2$ levels in Corpus Christi Bay, it cannot be determined if the CO_2 concentrations found in this study are typical or not. Meteorological data for September, 2018 shows a total rainfall of 33.9 cm compared to a historical average of 12.7 cm (NOAA, 2019). Agricultural runoff after a rain event can lead to nitrogen-loading in river waters. Increased nitrogen-loading into Corpus Christi Bay after this period of high rain could have increased primary production. An increase in primary production will increase CO_2 consumption in surface waters and decrease $p\text{CO}_2$ levels.

Yearly-averaged flow rate for the Nueces River (USGS Water Resources, 2019a) is shown in Figure 14. From preliminary values, it appears that the total volumetric flow rate for the year 2018 was particularly high; 2010 to 2017 mean flowrate was $2.5 \text{ m}^3 \text{ s}^{-1}$ versus 2018 mean flowrate of $15 \text{ m}^3 \text{ s}^{-1}$. Preliminary monthly average flows for the Nueces river for the year 2018 (USGS Water Resources, 2019a) are shown in Figure 15. River flow rate for Oct-Dec 2018, when this study took place, was significantly higher ($54 \text{ m}^3 \text{ s}^{-1}$) than Jan-Sep 2018, ($1.7 \text{ m}^3 \text{ s}^{-1}$). Data from this flow meter are not yet verified for publication; however, stations located upstream also showed a dramatic increase in river flow for the last four months of 2018 (USGS Water Resources, 2019b).

It is possible that high riverine input into the estuary caused uncharacteristically low surface $p\text{CO}_2$ values due to surface hypoxia caused by salinity-driven water column stratification. Additionally, Figure 16 shows water temperature from a NOAA/National Ocean Service (NOS) station located in close proximity to Corpus Christi Bay, for the end of 2018. There is an approximate 10°C decrease in surface water temperature from September to November (CO-OPS, 2019a). Decreases in surface water temperature, associated with seasonal changes, have been shown to cause an overall decrease in microbial activity (Sintes et al., 2010). A decrease in microbial activity could lower surface water $p\text{CO}_2$ as remineralization rate of organic carbon decreases.

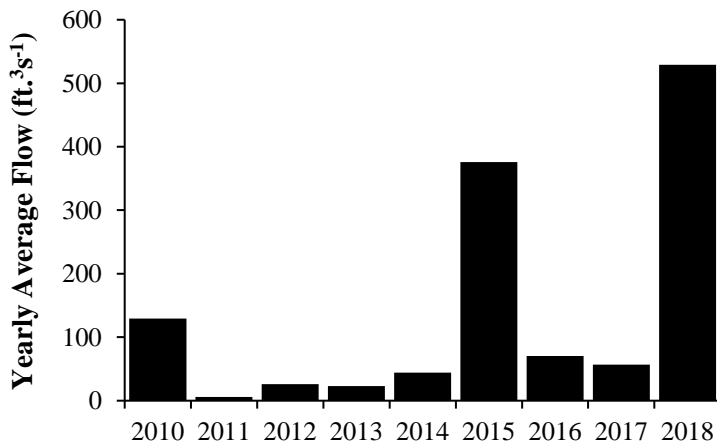


Figure 14 Yearly average flowrate for the Nueces River from USGS station 08211500 Nueces Rv at Calallen, TX. Values for 2018 are not yet approved for publication (USGS Water Resources, 2019a).

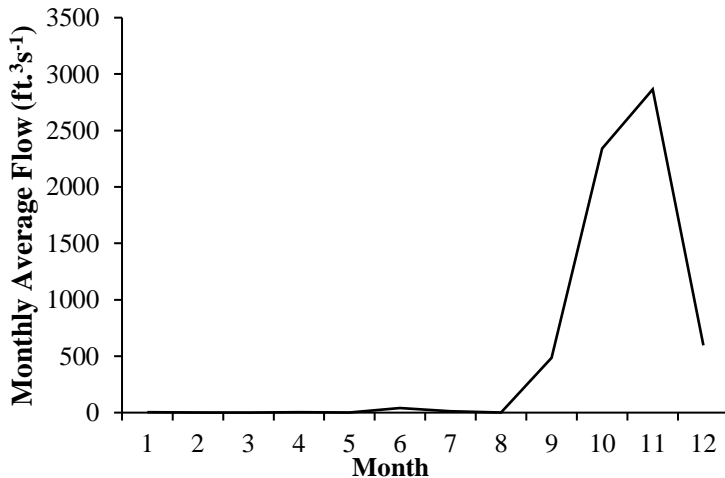


Figure 15 Monthly average flowrate for the Nueces River from USGS station 08211500 Nueces Rv at Calallen, TX. Values for 2018 are not yet approved for publication (USGS Water Resources, 2019a).

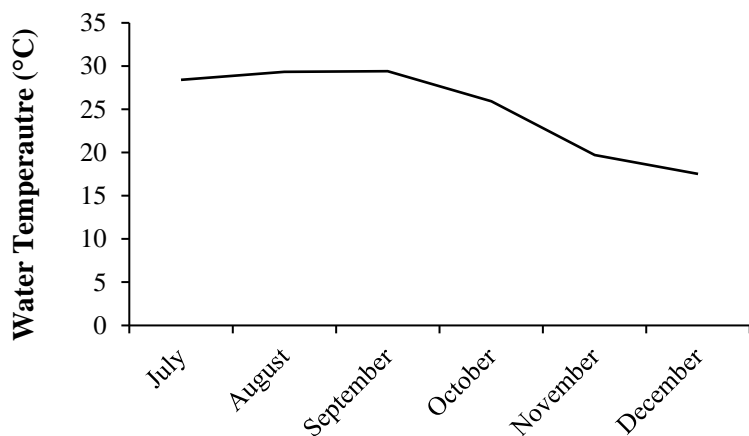


Figure 16 Monthly average temperatures for the end of 2018 from a NOAA/ National Ocean Service station 8775870 Bob Hall Pier, Corpus Christi, TX (CO-OPS, 2019a)

III.2 Gas Transfer Velocity

The gas transfer velocity, k , was calculated from Equation 3 using the reported flux, $p\text{CO}_2$ in the atmosphere and sea surface, and the solubility constant, K_0 , calculated from Weiss (1974). Gas transfer velocities were normalized to a Schmidt number of 660 using the information from Wanninkhof (2014), and Equation 8. Both the Schmidt number normalization and the solubility constant calculation are water-temperature and salinity dependent. Water temperature readings were taken from the SAMI- CO_2 sensor and salinity was assumed to be constant for the entire period at a value of 21.4 (from discrete water sample taken on 11/21/18). CO_2 concentrations were reported in dry-mole fraction (ppm), conversion to partial pressure for use in Equation 3 requires the dry-atmospheric pressure i.e. barometric pressure minus the vapor pressure of water (saturation pressure of water at SST multiplied by the relative humidity). The vapor pressure of seawater was calculated using data from Weiss and Price (1980), using sea temperature and a salinity of 21.4 and the relative humidity measured by the LiCor-7500. A complete set of sample calculations can be found in Appendix A.

Molar concentrations of CO_2 in both the atmosphere and the sea surface are shown in Figure 17. Atmospheric CO_2 concentration was higher than sea surface CO_2 concentration for all but two periods. Sea surface $p\text{CO}_2$ was obtained from the SAMI- CO_2 sensor. A discrete water

sample taken at 3 PM on 11/07/2018 showed a calculated $x\text{CO}_2$ value of 407.4 ppm. The corresponding reading from the SAMI- CO_2 was 427.5 ppm. Agreement of ± 20 ppm is typical for readings between these two methods (McCutcheon et al., in prep). Atmospheric CO_2 concentration was obtained from the LiCor-7500 analyzer as part of the eddy covariance setup. The instrument was not calibrated prior to deployment. However, as part of their ocean acidification program, NOAA has a sampling buoy located ~40 miles southwest of Port Fourchon in the Gulf of Mexico (NOAA PMEL Carbon Program, 2019). The station reads atmospheric and sea surface CO_2 concentrations. Atmospheric CO_2 concentration at the buoy location should be representative of the bulk CO_2 concentration for air in the Gulf of Mexico due to its distance from land-based anthropogenic CO_2 point sources. Agreement between the CO_2 measured at the buoy and at the study site is shown in Figure 18. The two measurement methods show good agreement for all but two periods (11/17/2018 and 11/18/2018) shown as A and B on Figure 18. These periods correspond to rapid wind direction changes from southeasterly to northwesterly and northeasterly, respectively.

Review of the study site from Figure 8 shows that winds from the northeast and the northwest are onshore winds and blow air over industrial areas before reaching the study site. Winds from the east to the south move air from the Gulf of Mexico to the study site without passing over land. CO_2 record from the NOAA-Coastal LA station and the local LiCor-7500 agreed when winds were southeasterly, indicating that the atmospheric CO_2 concentration as reported by the LiCor-7500 is accurate. The relationship between wind direction and atmospheric CO_2 concentration for the periods marked A and B in Figure 18, is shown in Figure 19.

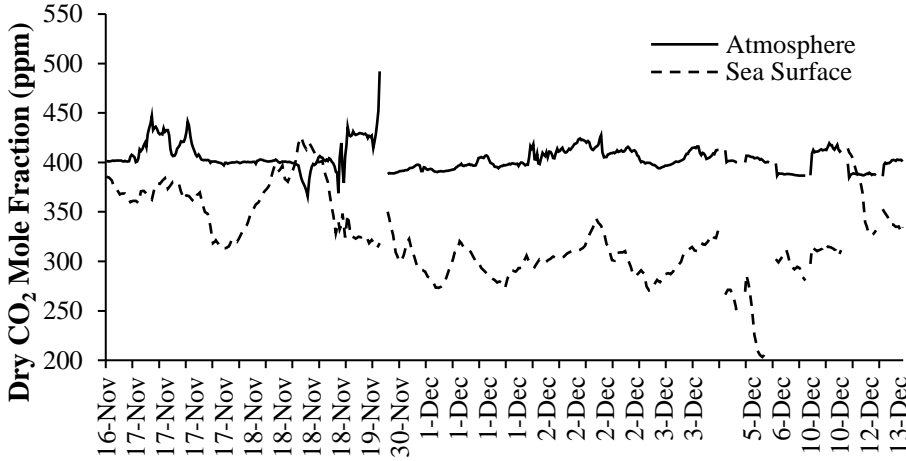


Figure 17 Dry mole concentrations of CO₂ in both the atmosphere and the sea surface.

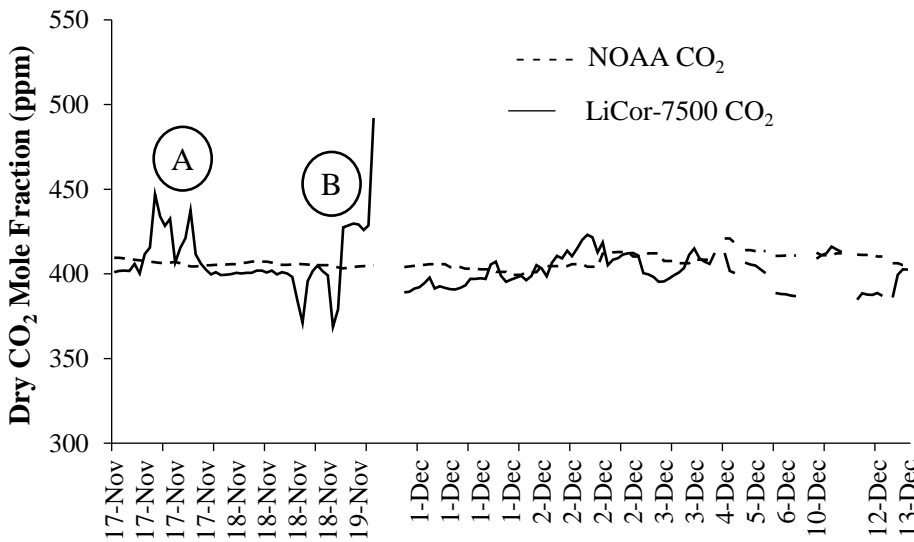


Figure 18 Dry mole concentrations of CO₂ from the LiCor-7500 analyzer and the NOAA buoy off the coast of Louisiana.

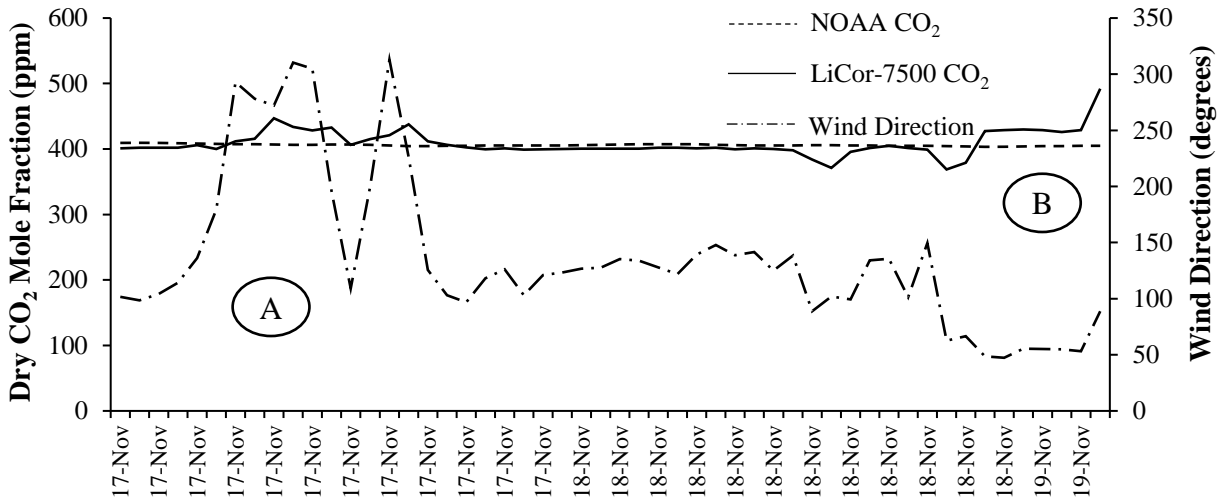


Figure 19 Relationship between wind direction (north = 0°), NOAA-Coastal LA and local CO₂ concentrations. Rapid direction change from southeasterly winds to northeasterly/northwesterly winds corresponds to divergence in CO₂ readings

Hourly-averaged k_{660} values for the entire period of deployment are shown in Figure 20. Gas transfer speeds should always be greater than zero. However, Figure 20 shows periods where the calculated k_{660} values were negative. This is due to periods where the measured CO₂ flux and $\Delta p\text{CO}_2$ values had opposite signs (Fig. 21). There are a number of potential sources for the disagreement in signs. The SAMI-CO₂ sensor took measurements every 30 minutes whilst the LiCor-7500 was running at a frequency of 20 Hz. As such, $\Delta p\text{CO}_2$ was calculated every 30 minutes and represents an instantaneous value for the concentration gradient whilst flux was calculated 20 times a second and reported as an average of the gas movement within a 15-minute period. Discrepancies between instantaneous flux direction and average flux direction could lead to sign disagreement. Additionally, periods of atmospheric instability and steep wind angle can lead to errors in the calculated flux (Burba, 2005). To avoid confusion and to remove potentially erroneous data, only positive k_{660} values were used in the subsequent transfer velocity calculations.

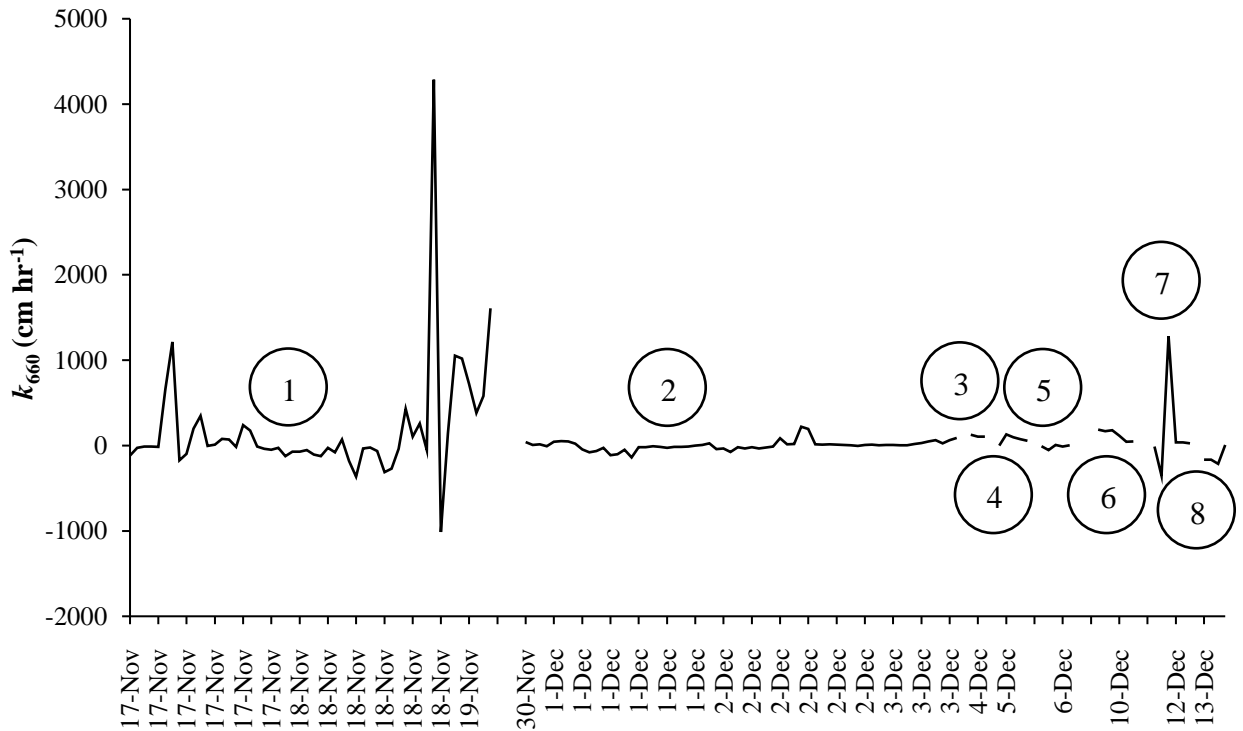


Figure 20 Hourly-average gas transfer velocities for the entire period of deployment. Velocities are normalized to a Schmidt number of 660. Numbers beside segments correspond to time ranges detailed in Table 2.

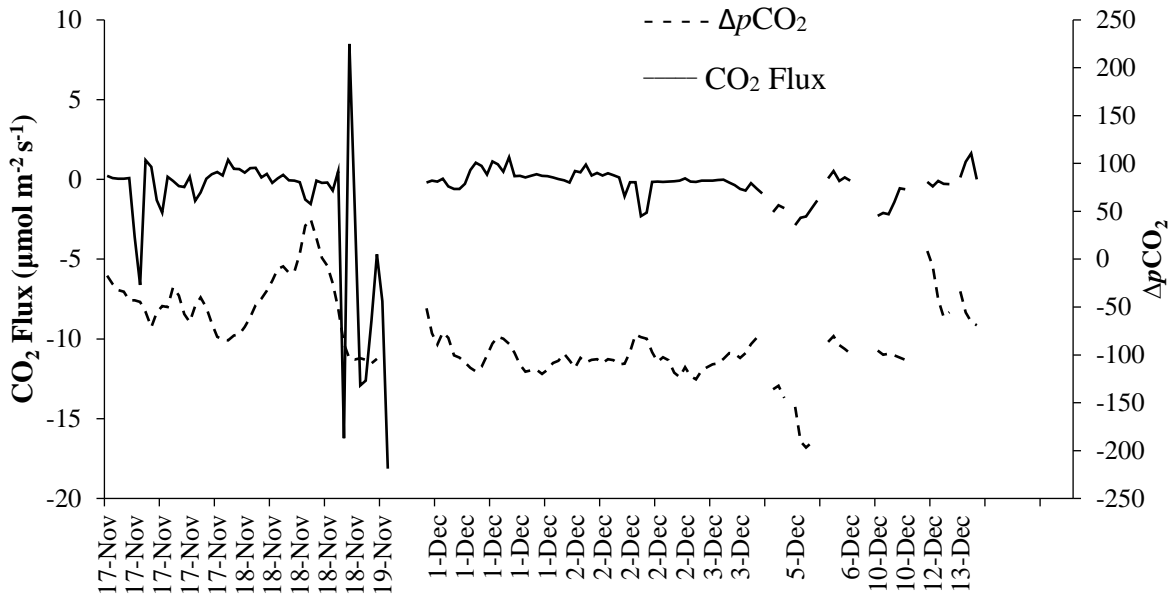


Figure 21 Time series of CO₂ flux and ΔpCO₂.

The relationship between positive hourly-averaged values of k_{660} and wind speed at 10 m about the sea surface for the complete wind speed range is shown in Figure 22.

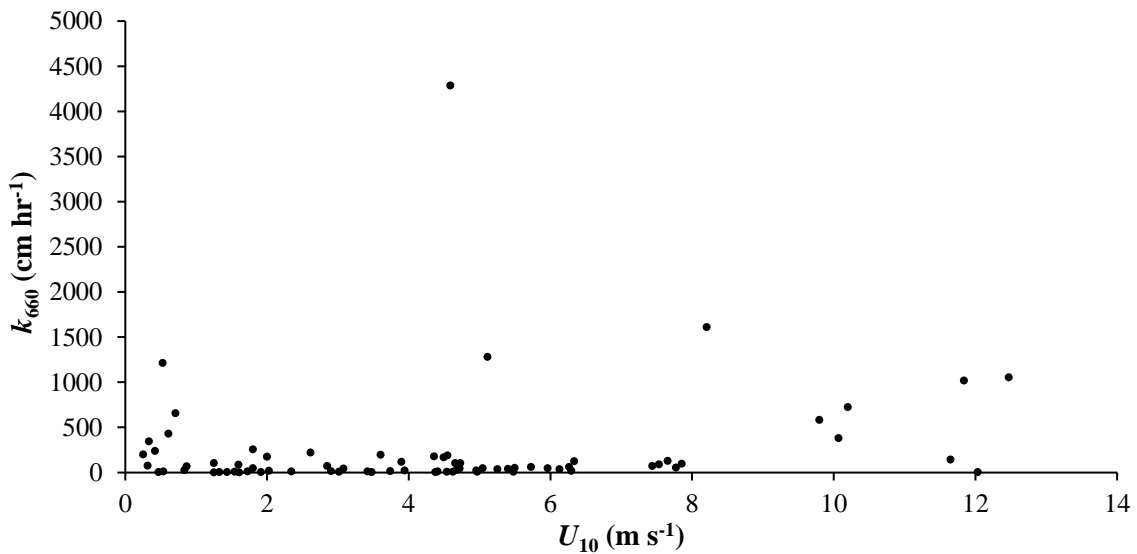


Figure 22 Positive hourly average of values of k_{660} vs. U_{10} for complete wind speed range with no outliers removed

The dependence of gas transfer velocity on wind speed varies depending on the magnitude of wind speed (Liss and Merlivat, 1986). At low wind speeds ($< 3.6 \text{ m s}^{-1}$), factors other than

wind-driven turbulence become more important in determining gas transfer velocity. This is thought to be especially true for shallow, coastal waters where bottom-driven turbulence due to tidal motions can play a large role in moderating gas transport under low wind shear conditions. Therefore, to develop a model for gas transfer velocity based on external factors, the data will be broken into two wind speed regimes.

The relationship between gas transfer velocity and wind speed for low wind speeds is shown in Figure 23. A linear model for k_{660} has an R^2 value of 0.1479.

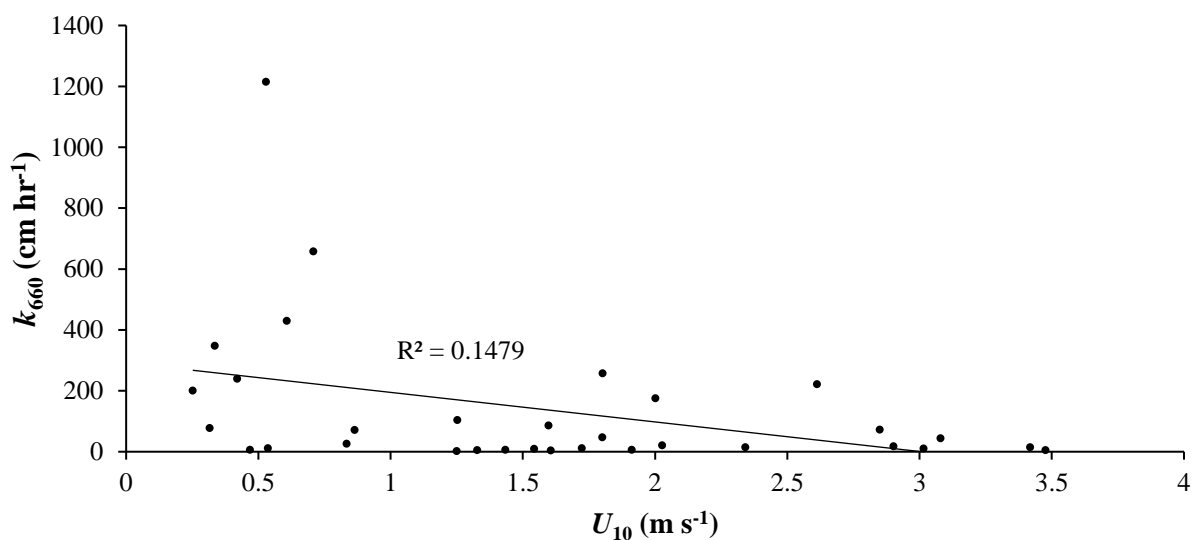


Figure 23 Positive values of k_{660} versus wind speed at 10 m for wind speeds below 3.6 m s⁻¹ and linear best fit with an R^2 value of 0.1479.

Interestingly, gas transfer velocity appears to have an inversely proportional relationship to wind speed at low wind speeds. However, as this is the low wind speed regime, other factors are expected to strongly influence gas transport particularly surface turbulence caused by water shear. This can be seen by the low R^2 value indicating that wind speed accounts for only ~ 15% of gas transfer. Water velocity data were unavailable for this study, as a proxy tidal information from NOAA/NOS monitoring station 8775296 USS Lexington, Corpus Christi Bay, TX, is used (CO-OPS, 2019b). Tidal information is reported as water level readings taken every hour. This

was converted to water speed in the vertical direction by dividing the difference between adjacent height measurements by 60 minutes. Although this gives water velocity in the vertical direction and not the horizontal, for a fixed volume (i.e. the Bay) these two numbers should be proportional.

Analysis of tidal patterns and gas transfer velocity reveals no definitive relationship (Figure 24). A linear model of the two variables returns an R^2 value of 0.0014. However, use of tidal patterns as a proxy for water shear is problematic for several reasons, including the presence of a diurnal trend in wind speeds, which mimic the diurnal tidal patterns. Diurnal variations in wind speed and water level for Corpus Christi Bay from 11/30/18 to 12/3/18 are shown in Figure 25.

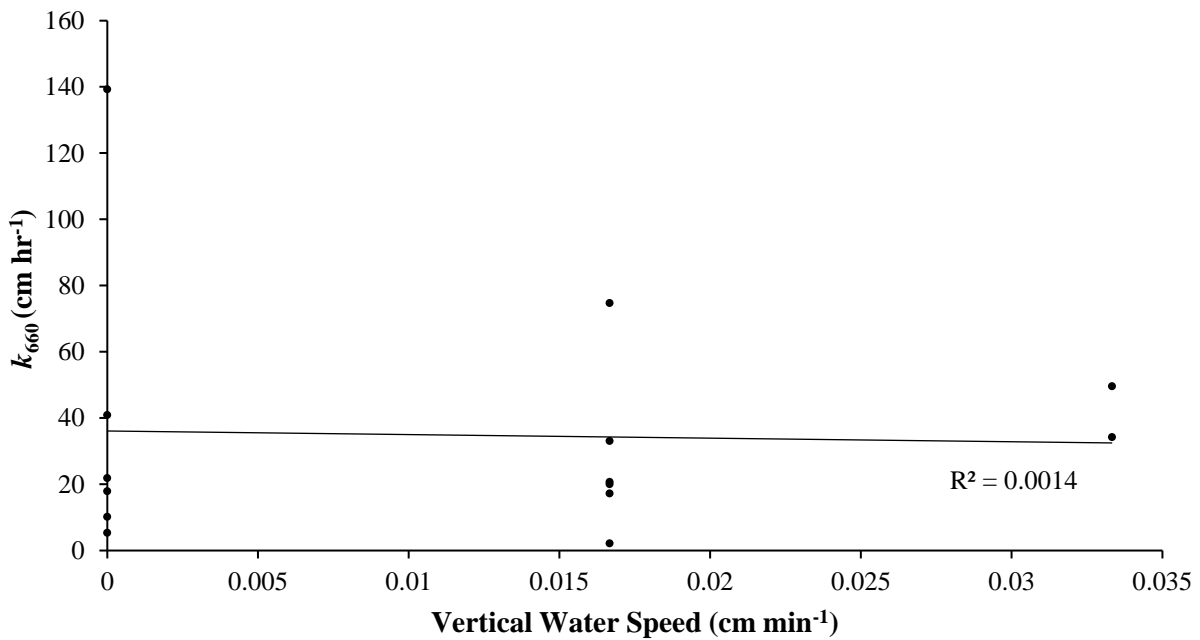


Figure 24 k_{660} versus vertical water speed for wind speeds below 3.6 m s⁻¹.

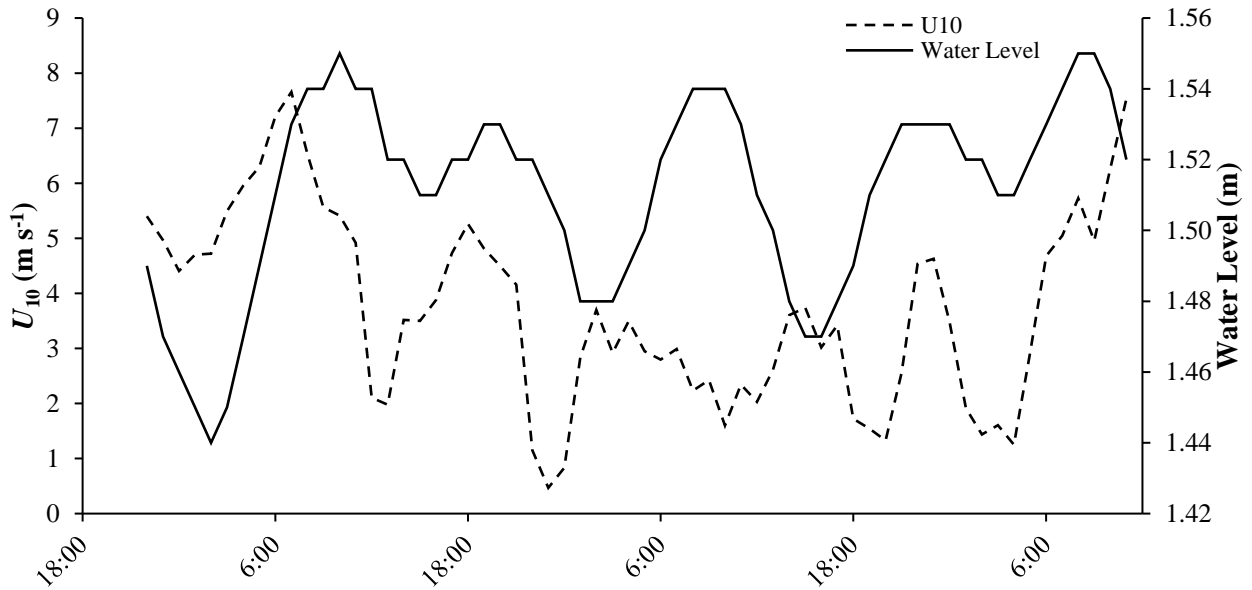


Figure 25 Diurnal trend of wind speed and astronomical tide for Corpus Christi Bay (CO-OPS, 2019b), from 11/30/18 at 10 PM until 12/03/18 at 11 AM.

Diurnal trends in coastal marine winds have been demonstrated by other groups and are, generally, a result of the thermal capacity of water affecting air temperature, resulting in differences in air pressure onshore and offshore (Lapworth, 2005).

For wind speeds above 3.6 m s^{-1} , the relationship between gas transfer velocity and wind speed becomes better defined. The resulting relationship between k_{660} and wind speed is shown in Figure 26. After bin-averaging, removal of negative k_{660} values, and removal of outliers there were a total of 40 measurements of gas transfer velocity at wind speeds ranging from 3.6 m s^{-1} to 12.5 m s^{-1} . The bulk (75%, $N=30$) of the data are for wind speeds below 7.6 m s^{-1} . With 15% ($N=6$) of the data occurring at wind speeds above 10 m s^{-1} . A total of three outliers were removed, two of these outliers corresponded to the period of instability on 11/18/18 that was previously discussed, and an additional outlier was removed from a period of equipment instability immediately after startup on 12/12/2018.

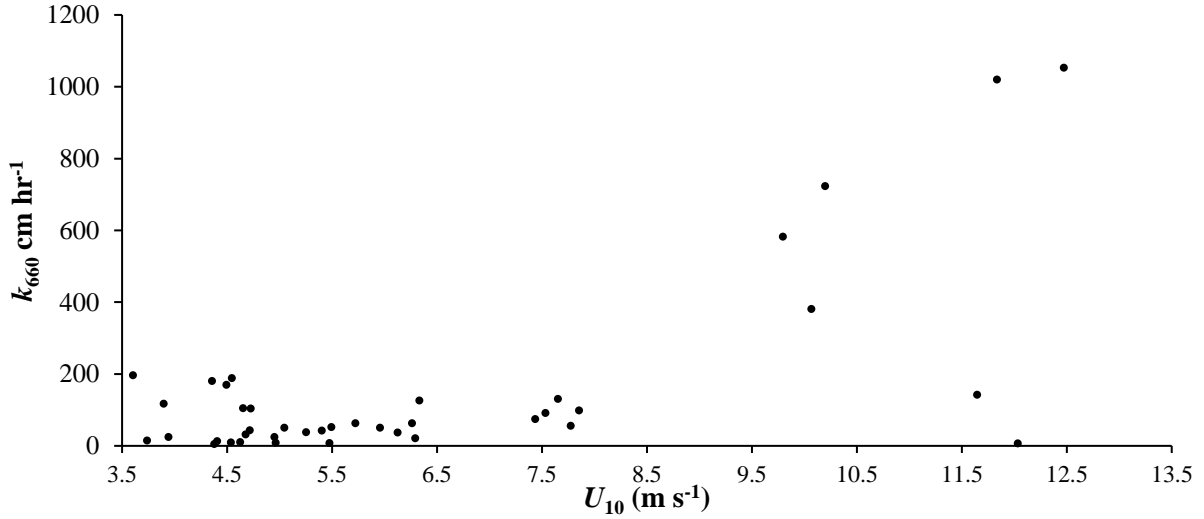


Figure 26 Relationship between absolute value of k_{660} and wind speed for wind speeds above 3.6 m s^{-1} with three outliers removed.

To determine the best mathematical model between k_{660} and U_{10} for $U_{10} > 3.6 \text{ m s}^{-1}$, several models were tested (Table 4).

Table 4 Comparison of models for relationship between k_{660} and U_{10} for $U_{10} > 3.6 \text{ m s}^{-1}$.

Number	Model	Results	Adjusted R^2	Residual Std. Error
1	$y = ax + b$	$k_{660} = 67.2 U_{10} - 274$	0.4364	190
2	$y = ax$	$k_{660} = 29.8 U_{10}$	0.4725	213
3	$y = ax^2 + b$	$k_{660} = 4.45 U_{10}^2 - 54.6$	0.4830	182
4	$y = ax^2$	$k_{660} = 3.77 U_{10}^2$	0.6108	183
5	$y = ax^3 + b$	$k_{660} = 0.35 U_{10}^2 + 14.9$	0.5030	178
6	$y = ax^3$	$k_{660} = 0.36 U_{10}^3$	0.6385	176
7	$y = a \cdot \exp^x$	$k_{660} = 2.3 \cdot \exp[0.27U_{10}]$	0.2272	NA

Based on adjusted R^2 and residual standard error values a cubic model (Model 6) with the intercept fixed at 0 shows the best fit between wind speed and gas transfer velocity. Although measurements below 3.6 m s^{-1} did not contribute to this model, fixing the intercept at 0 means that at wind speeds of 0 m s^{-1} , wind-induced gas transfer is also 0 which is realistic.

Therefore, Equation 13 (hereafter referred to as C19) represents the chosen model for k_{660} as a function of U_{10} for $3.6 \text{ m s}^{-1} < U_{10} < 12.5 \text{ m s}^{-1}$:

$$k_{660} = 0.36U_{10}^3 \quad (13)$$

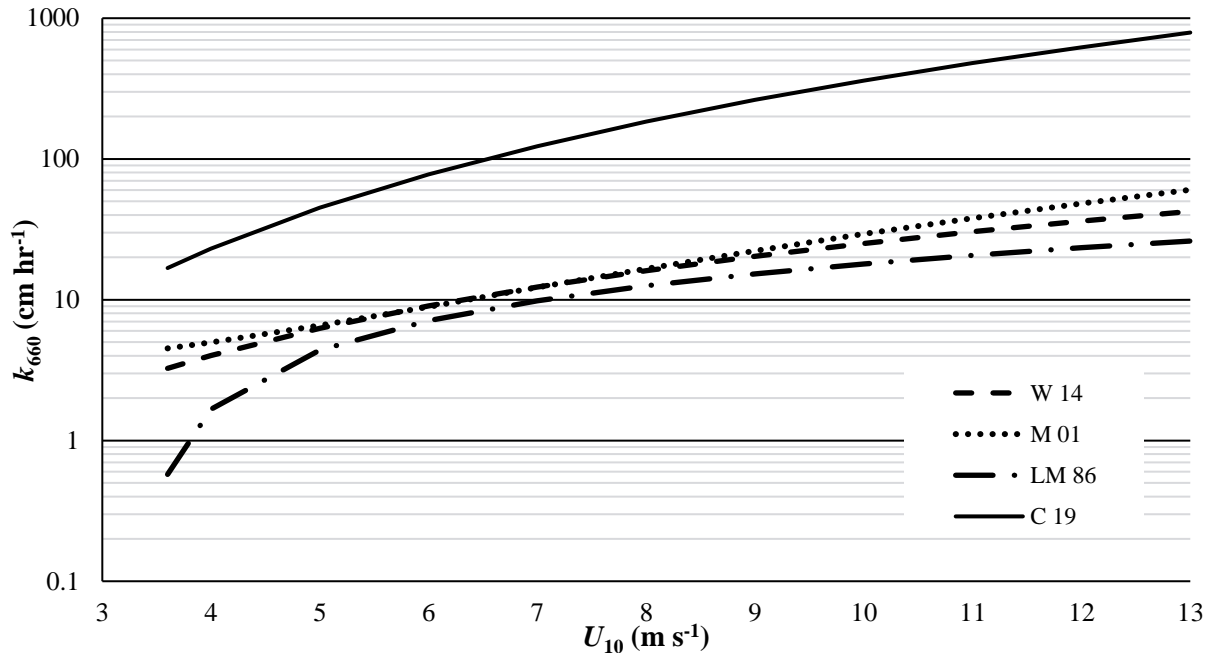


Figure 27 Comparison of gas transfer model generated by this study (C 19) and models (W14) Wanninkhof (2014), (M01) McGillis et al. (2001), and (LM 86) Liss and Merlivat (1986).. k_{660} axis is in \log_{10} .

The model generated in this study predicts a gas transfer velocity approximately an order of magnitude greater than the corresponding models for the open ocean (Fig. 27). The increase in measured gas transfer velocity as a function of wind speed may be due to inherent differences between gas kinetics in the open ocean versus coastal waters.

To better understand the gas transfer velocities predicted by this model for coastal regions, two additional models were taken from literature that describe the dependence of k_{660} on wind speed. Model B04 is from work published by Borges et al. (2004), which studied gas transfer in the Scheldt Estuary using the floating chamber method. The bulk (61%) of their measurements were taken at wind speeds between 3 and 7 m s^{-1} with only 4.4% of their measurements taken at wind speeds above 10 m s^{-1} (maximum wind speed 11 m s^{-1}). Borges et al. (2004), took measurements at three different locations with water depth varying from 8.6 m to 14.7 m. The model C95 is taken from Clark et al. (1995), who used the dual tracer method to determine trace

gas flux in the Hudson river. Mean wind speeds for this study were from 0.7 m s^{-1} to 5.1 m s^{-1} with no data collected at wind speeds above 7 m s^{-1} . Additionally, measurements were taken at depths from 4 m to 9 m. The comparison between the C19 model and the two coastal models is shown in Figure 28.

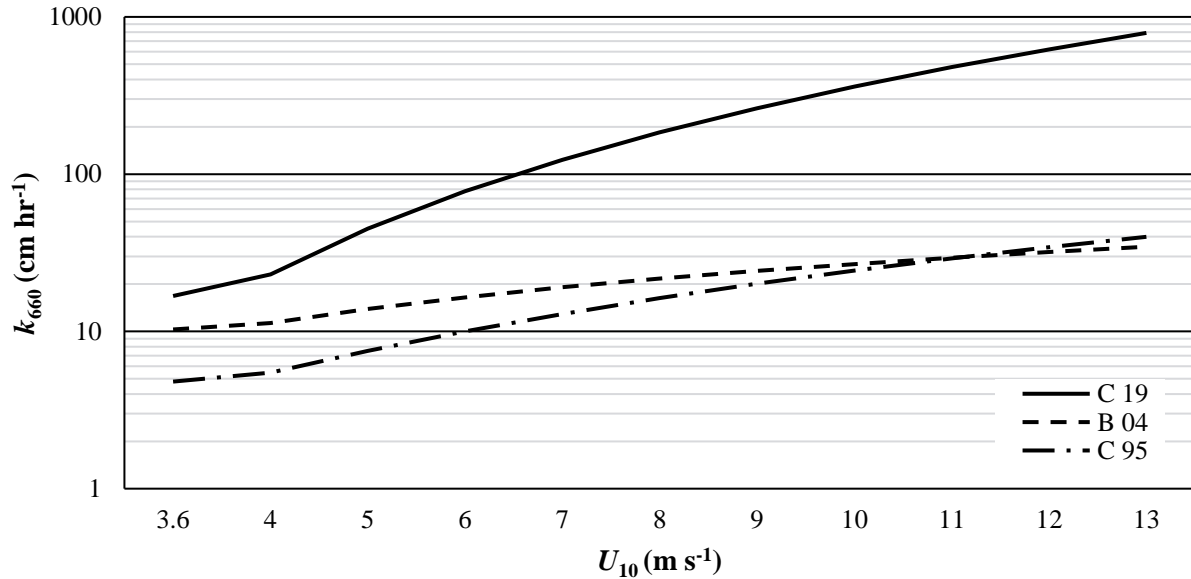


Figure 28 Comparison of model C19 with models for k_{660} vs. wind speed for coastal regions.

It can be seen that the model generated in this study is still approximately an order of magnitude greater than the existing models found in the literature with greater divergence occurring at higher wind speeds. This could be as a result of the relatively shallow depth at which this study was conducted (mean water level 1.5 m). Gas transfer velocity has been shown to vary inversely with water depth, h , where $k \propto h^{-0.5}$. So, it would be expected that gas transfer measurements taken at 1.5 m would be ~ 3 times greater than measurements taken at 11.7 m (mean depth B04) and ~ 2 times greater than measurements taken at 6.5 m (mean depth C95).

Additionally, maximum wind speed modeled in B04 was 11 m s^{-1} and 7 m s^{-1} in C95. As shown for the open ocean, gas transfer has a higher dependence on wind speed at higher wind speeds due to the presence of entrained air, i.e., whitecaps (McGillis et al., 2001; Monahan and Spillane, 1984).

III.3 Floating Chamber Correction

Due to difficulties with power supply and rough water conditions, only three measurements of flux were successfully taken using the floating chamber. Comparison of the flux recorded using both the eddy covariance (EC) and floating chamber (FC) are shown in Figure 29. For all three measurements, the FC method overestimated flux by between 1.5 to 4.6 times. However, there is no clear correlation between the discrepancy in measurements and wind speed. Additionally, there was an occasion when the FC measured net CO₂ movement to be into the estuary and the EC measured net movement to be to the atmosphere.

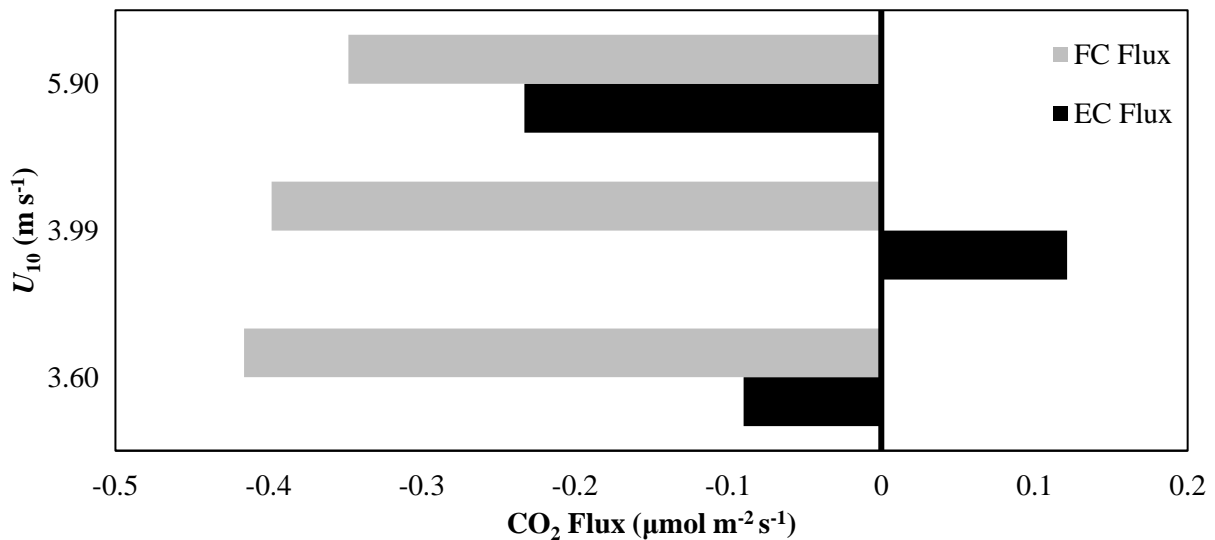


Figure 29 Comparison of FC and EC results versus wind speed.

Differences between measurements for the two methods are generally shown to be due to inaccuracies with the FC method (Borges et al., 2004; Frankignoulle et al., 1998; Raymond and Cole, 2017). At low wind speeds, the weight of the FC on the water surface can cause localized turbulence which will artificially increase measured gas flux above the true value. At moderate to high wind speeds, the walls of the FC will shelter the sea surface from the wind. This can lead to a decrease in measured gas transfer as surface renewal rate is decreased.

IV. RECOMMENDATIONS

During the course of this experiment, Corpus Christi Bay acted as both a source and a sink of CO₂ to the atmosphere, intermittently. Variations in estuarine surface $p\text{CO}_2$ can occur due to diurnal changes in photosynthesis and respiration rates, seasonal changes in microbial activity, and changes in volume and concentration of nutrient and DIC input from freshwater influx. Due to the relatively small difference in atmospheric and surface water $p\text{CO}_2$, any moderate fluctuation in CO₂ consumption, production, or accumulation could easily lead to a change in net CO₂ movement. In order to determine the overall role of Corpus Christi Bay in the local carbon cycle, year-round monitoring of surface water $p\text{CO}_2$ should lead to a better understanding of the response of the carbonate system to these external factors.

This study would benefit greatly from being repeated with water speed measurements in three-dimensions. Such measurements can be taken with an acoustic doppler velocimeter (Figure 31). The probe uses the scattering properties of particles found naturally in the water to determine the velocity component in all three space dimensions. Water velocity data should enable gas transfer at low wind speeds to be modeled and will enhance modelling at moderate and high wind speeds.

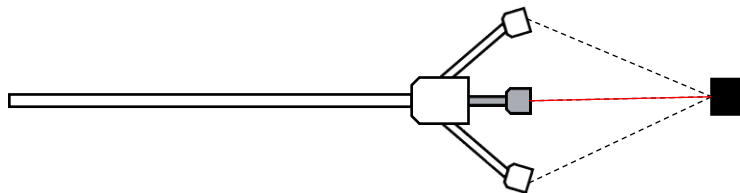


Figure 30 Acoustic doppler velocimeter. Solid red line represents single transmitted acoustic signal. Signal scattered by naturally occurring particles in sample volume, scattered signal (dashed black lines) received by three receivers set at 120° from each other. Doppler shift of scattered signal gives three-dimensional velocity profile of water.

The floating chamber method should be developed further to determine its viability as a direct flux measuring technique. Further measurements taken with the chamber and directly

compared to EC measurements should allow for a more detailed comparison between the two methods. Additionally, constructing a more robust floating platform for the chamber to rest on would remove the need for manual handling which would allow for measurements to be taken at higher wind speeds and rougher water conditions.

V. CONCLUSIONS

V.1 CO₂ Flux

Surface water $x\text{CO}_2$ values have been measured as high as 5,700 ppm in some estuaries (Frankignoulle et al., 1996). The relatively modest $x\text{CO}_2$ values measured during this study, and by Yao and Hu (2017), are generally within ± 100 ppm of the atmospheric concentration of CO_2 . Maximum surface water $x\text{CO}_2$ value during this study was 425.7 ppm (11/18/18) and minimum was 203.3 ppm (12/5/2018) giving a maximum fluctuation of 222.4 ppm. Fluctuations in $x\text{CO}_2$ of this magnitude coupled with relatively small differences in atmospheric and estuarine $x\text{CO}_2$ values could cause a net heterotrophic estuary to become autotrophic, and vice versa. Due to the short deployment of the EC equipment, it is not possible to make long-term statements about the flux patterns of Corpus Christi Bay using the data collected in this study. Yao and Hu (2017), also describe nearby MAE as a net CO_2 sink during the winter months but they found it to be a net CO_2 source during the summer. Additionally, unusually large precipitation rates and freshwater inputs to the bay and decreasing surface water temperature prior to this study may have caused $p\text{CO}_2$ levels to fall below typical levels.

Despite small $\Delta p\text{CO}_2$ values, average CO_2 flux was still high ($-23.3 \text{ mmol C m}^{-2} \text{ d}^{-1}$) compared to the global average ($-0.164 \text{ mmol C m}^{-2} \text{ d}^{-1}$). This is due to strong kinetic factors including high winds experienced at the study site.

V.2 Gas Transfer Velocity

Gas transfer velocity was modeled as a function of wind speed. The resulting best fit model showed a cubic dependence of gas transfer velocity on wind speed. The final model is only valid for wind speeds above 3.6 m s^{-1} and explains approximately 64% of the gas transfer.

At wind speeds below 3.6 m s^{-1} , only 15% of gas transport is due to wind shear. Other factors, including surfactant contribution and water shear account for the other 85% of gas transfer.

The model developed by this study predicts gas transfer to be approximately an order of magnitude greater than corresponding studies. This is potentially due to the increased effect of bottom driven turbulence at the study site owing to shallow water conditions. Additionally, this study included stronger winds than the corresponding coastal studies. Dependence on gas transfer with wind speed is known to increase with increasing wind speeds.

V.3 Floating Chamber Comparison

The floating chamber method overestimated flux across all three measurements. However, a clear relationship between the magnitude of overestimation and wind speed was not apparent. This is most likely due to the small sample of FC measurements. Additionally, measurements made at higher wind speeds were more difficult to make due to the increased quantity and energy of waves.

Despite difficulties in obtaining FC measurements, due to the simple and inexpensive nature of the FC, both to construct and operate, it is still worth perusing as a viable option for direct flux measurements.

REFERENCES

- Alvarez, M., Fernandez, E., Reza, F.F.P., 1999. Air-sea CO₂ fluxes in a coastal embayment affected by upwelling: physical versus biological control. *Oceanol. Acta* 22, 449–515.
- Applebaum, S., Montagna, P.A., Ritter, C., 2005. Status and trends of dissolved oxygen in Corpus Christi Bay, Texas, U.S.A. *Environ. Monit. Assess.* 107, 297–311.
- Asher, W.E., Pankow, J.F., 1991. Prediction of gas/water mass transport coefficients by a surface renewal model. *Environ. Sci. Technol.* 25, 1294–1300.
- Baldocchi, D.D., 2003. Assessing the eddy covariance technique for evaluating carbon dioxide exchange rates of ecosystems: past, present and future. *Glob. Chang. Biol.* 479–492.
- Bastviken, D., Sundgren, I., Natchimuthu, S., Reyier, H., Gålfalk, M., 2015. Technical Note: Cost-efficient approaches to measure carbon dioxide fluxes and concentrations in terrestrial and aquatic environments using mini loggers. *Biogeosciences* 12, 3849–3859.
- Bauer, J.E., Cai, W.J., Raymond, P.A., Bianchi, T.S., Hopkinson, C.S., Regnier, P.A.G., 2013. The changing carbon cycle of the coastal ocean. *Nature* 504, 61–70.
- Benway, H.M., Doney, S.C., 2014. Scientific Outcomes and Future Challenges of the Ocean Carbon and Biogeochemistry Program. *Oceanography* 27, 106–107.
- Borges, A.V., Vanderborcht, J.-P., Schiettecatte, L.-S., Gazeau, F., Ferrón-Smith, S., Delille, B., Frankignoulle, M., 2004. Variability of the gas transfer velocity of CO₂ in a macrotidal estuary (the Scheldt). *Estuaries* 27, 593–603.
- Borges, A. V., 2005. Do we have enough pieces of the jigsaw to integrate CO₂ fluxes in the coastal ocean? *Estuaries* 28, 3–27.
- Broecker, W.S., Peteet, D.M., Rind, D., 1985. Does the ocean-atmosphere system have more than one stable mode of operation? *Nature* 315, 21–26.

- Burba, G., 2005. Eddy Covariance Method for Scientific, Industrial, Agricultural and Regulatory Applications, 1st ed, Li-Cor Biosciences. LiCor, Lincoln.
- Cai, W., Wang, Y., 1998. The chemistry, fluxes, and sources of carbon dioxide in the estuarine waters of the Satilla and Altamaha Rivers, Georgia. *Limnol. Oceanogr.* 43, 657–668.
- Carter, B.R., Radich, J.A., Doyle, H.L., Dickson, A.G., 2013. An automated system for spectrophotometric seawater pH measurements. *Limnol. Oceanogr. Methods* 11, 16–27.
- Clark, J.F., Schlosser, P., Simpson, H.J., Stute, M., Wanninkhof, R., Ho, D.T., 1995. Relationship between gas transfer velocities and wind speeds in the tidal Hudson River determined by the dual tracer technique, in: Jahne, B., Monahan, E.C. (Eds.), *Air-Water Gas Transfer*. AEON Verlag: Hanau, Germany, Heidelberg, pp. 785–800.
- Clark, J.F., Wanninkhof, R.H., Schlosser, P., Simpson, H.J., 1994. Gas exchange rates in the tidal Hudson river using a dual tracer technique. *Tellus B* 46, 274–285.
- Clayson, C.A., Curry, J.A., 1996. Evaluation of turbulent fluxes at the ocean surface using surface renewal theory and where Bulk quoted number is that an accuracy of Wm^{-1} in the net surface frequency platform motions induced by the ocean . Bulk. *J. Geophys. Res.* 101.
- Clayton, T.D., Byrne, R.H., 1993. Spectrophotometric seawater pH measurements: total hydrogen ion concentration scale calibration of m-cresol purple and at-sea results. *Deep Sea Res. Part I Oceanogr. Res. Pap.* 40, 2115–2129.
- CO-OPS, 2019a. NOAA/NOS/CO-OPS Station 8775870 Bob Hall Pier, Corpus Christi TX <https://tidesandcurrents.noaa.gov/physocean.html?id=8775870> (accessed 3.3.19).
- CO-OPS, 2019b. NOAA/NOS/CO-OPS Station 8775296 USS Lexington, Corpus Christi Bay, <https://tidesandcurrents.noaa.gov/noaatidepredictions.html?id=8775296>
- Dai, M., Lu, Z., Zhai, W., Chen, B., Cao, Z., Zhou, K., Cai, W., Chenc, C.-T.A., 2009. Diurnal

- variations of surface seawater pCO₂ in contrasting coastal environments. *Limnol. Oceanogr.* 54, 735–745.
- Deacon, E.L., 1977. Gas transfer to and across an air-water interface. *Tellus* 29, 363–374.
- del Giorgio, P., Cole, J.J., Cimbleris, A., 1997. Respiration rates in bacteria exceed phytoplankton production in upproductive aquatic systems. *Nature* 385, 148–151.
- Dickson, A.G., 1990. Standard potential of the reaction: $\text{AgCl(s)} + 12\text{H}_2\text{(g)} = \text{Ag(s)} + \text{HCl(aq)}$, and the standard acidity constant of the ion HSO_4^- in synthetic sea water from 273.15 to 318.15 K. *J. Chem. Thermodyn.* 22, 113–127.
- Dickson, A.G., Sabine, C.L., Christian, J.R., 2007. Guide to best practices for ocean CO₂ measurements. North Pacific Marine Science Organization.
- Doney, S.C., Fabry, V.J., Feely, R.A., Kleypas, J.A., 2009. Ocean Acidification: The Other CO₂ Problem. *Ann. Rev. Mar. Sci.* 1, 169–192.
- Duc, N.T., Silverstein, S., Lundmark, L., Reyier, H., Crill, P., Bastviken, D., 2013. Automated flux chamber for investigating gas flux at water-air interfaces. *Environ. Sci. Technol.* 47, 968–975.
- Easterling, D.R., Meehl, G.A., Parmesan, C., Changnon, S.A., Karl, T.R., Mearns, L.O., 2000. Climate extremes: Observations, modeling, and impacts. *Science* (80-.). 289, 2068–2074.
- Frankignoulle, M., Abril, G., Borges, A., Bourge, I., Canon, C., Delille, B., Libert, E., Theate, J.-M., 1998. Carbon dioxide emissions from European estuaries. *Science* (80-.). 282, 434–436.
- Frankignoulle, M., Bourge, I., Wollast, R., 1996. Atmospheric CO₂ fluxes in a highly polluted polluted estuary (the Scheldt). *Limnol. Oceanogr.* 41, 365–369.
- Gruber, N., Clement, D., Carter, B.R., Feely, R.A., van Heuven, S., Hoppema, M., Ishii, M.,

- Key, R.M., Kozyr, A., Lauvset, S.K., 2019. The oceanic sink for anthropogenic CO₂ from 1994 to 2007. *Science* (80-.). 363, 1193–1199.
- Harte Research Institute, 2019. Corpus Christi Bay [WWW Document]. Gulf Base. URL <https://www.gulfbase.org/geological-feature/corpus-christi-bay>
- Hsu, S.A., Meindl, E.A., Gilhousen, D.B., 1994. Determining the power-law wind-profile exponent under near-neutral stability conditions at sea. *Am. Meteorol. Society* 33, 757–765.
- Hu, X., Pollack, J.B., McCutcheon, M.R., Montagna, P.A., Ouyang, Z., 2015. Long-term alkalinity decrease and acidification of estuaries in northwestern gulf of Mexico. *Environ. Sci. Technol.* 49, 3401–3409.
- Jähne, B., Haußecker, H., 1998. Air-water gas exchange. *Annu. Rev. Fluid Mech.* 30, 443–468.
- Jähne, B., Heinz, G., Dietrich, W., 1987. Measurement of the diffusion coefficients of sparingly soluble gases in water. *J. Geophys. Res. Ocean.* 92, 10767–10776.
- Lapworth, A., 2005. The diurnal variation of the marine surface wind in an offshore flow. *Q. J. R. Meteorol. Soc.* 131, 2367–2387.
- Lewis, E., Wallace, D.W.R., 1998. Program developed for CO₂ system calculations. Oak Ridge.
- Liss, P.S., Merlivat, L., 1986. Air-Sea Gas Exchange Rates: Introduction and Synthesis, in: Buat-Menard, P. (Ed.), *The Role of Air-Sea Exchange in Geochemical Cycling*. Springer Science & Business Media, Dordrecht, pp. 113–127.
- Martinsen, K.T., Kragh, T., Sand-Jensen, K., 2018. A simple and cost-efficient automated floating chamber for continuous measurements of carbon dioxide gas flux on lakes. *Biogeosciences Discuss.* 25, 1–12.
- McCutcheon, M., Hu, X., et al., Texas A&M University, Corpus Christi, *In Prep* 2019
- McGillis, W.R., Edson, J.B., Ware, J.D., Dacey, J.W.H., Hare, J.E., Fairall, C.W., Wanninkhof,

- R., 2001. Carbon dioxide flux techniques performed during GasEx-98. *Mar. Chem.* 75, 267–280.
- Millero, F.J., 2010. Carbonate constants for estuarine waters. *Mar. Freshw. Res.* 61, 139–142.
- Monahan, E.C., Spillane, M.C., 1984. The role of oceanic whitecaps in air-sea gas exchange., in: Brutsaert, W., Jirka, G.H. (Eds.), *Gas Transfer at Water Surfaces*. Springer Science & Business Media, Dordrecht, pp. 495–496.
- NOAA, 2019. National Weather Service Forecast Office Corpus Christi, TX [WWW Document]. URL <https://w2.weather.gov/climate/index.php?wfo=crp> (accessed 3.3.19).
- NOAA, 2018. Carbon Dioxide | Vital Signs – Climate Change: Vital Signs of the Planet [WWW Document]. [nasa.gov](https://climate.nasa.gov/vital-signs/carbon-dioxide/). URL <https://climate.nasa.gov/vital-signs/carbon-dioxide/> (accessed 1.27.18).
- NOAA PMEL Carbon Program, 2019. Coastal LA <https://www.pmel.noaa.gov/co2/story/Coastal+LA> (accessed 2.27.19).
- NOAA PMEL Carbon Program, 2000. CO₂ Flux Map <https://www.pmel.noaa.gov/co2/file/CO2+Flux+Map> (accessed 2.28.19).
- Orlando, S.P.J., Rozas, L.P., Ward, G.H., Klein, C.J., 1993. Salinity Characteristics of Gulf of Mexico Estuaries. *Natl. Ocean. Atmos. Adm. Off. Ocean Resour. Conserv. Assess.* 209.
- Port Authority of Corpus Christi, 2012. Intercoastal Waterways: Port of Corpus Christi [WWW Document]. URL <http://portofcc.com/capabilities/logistics/intercoastal-waterways/> (accessed 1.30.19).
- Raymond, P.A., Cole, J.J., 2017. Gas Exchange in Rivers and Estuaries: Choosing a Gas Transfer Velocity. *Coast. Estuar. Res. Fed.* 24, 312–317.
- Riebesell, U., Zondervan, I., Rost, B., Tortell, P.D., Zeebe, R.E., Morel, F.M., 2000. Reduced

- calcification of marine plankton in response to increased atmospheric CO₂. *Nature* 407, 364–7.
- Ritter, C., Montagna, P.A., 1999. Seasonal Hypoxia and Models of Benthic Response in a Texas Bay. *Estuaries* 22, 7.
- Rosenzweig, C., Karoly, D., Vicarelli, M., Neofotis, P., Wu, Q., Casassa, G., Menzel, A., Root, T.L., Estrella, N., Seguin, B., Tryjanowski, P., Liu, C., Rawlins, S., Imeson, A., 2008. Attributing physical and biological impacts to anthropogenic climate change. *Nature* 453, 353–357.
- Sabine, C.L., 2004. The Oceanic Sink for Anthropogenic CO₂. *Science* (80-). 305, 367–371.
- Sabine, C.L., Feely, R.A., Gruber, N., Key, R.M., Lee, K., Bullister, J.L., Wanninkhof, R., Wong, C.S., Wallace, D.W.R., Tilbrook, B., Millero, F.J., Peng, T.H., Kozyr, A., Ono, T., Rios, A.F., 2004. The oceanic sink for anthropogenic CO₂. *Science* (80-). 305, 367–371. h
- Sintes, E., Stoderegger, K., Parada, V., Herndl, G.J., 2010. Seasonal dynamics of dissolved organic matter and microbial activity in the coastal North Sea. *Aquat. Microb. Ecol.* 60, 85–95.
- Solomon, S., Plattner, G.-K., Knutti, R., Friedlingstein, P., 2009. Irreversible climate change due to carbon dioxide emissions. *Pnas* 106, 1704–1709.
- Solomon, S., Qin, D., 2013. *Climate Change 2007 The Physical Science Basis*, The Journal of Chemical Information and Modeling. Cambridge Univ. Press, Cambridge, UK, and New York.
- Takahashi, T., Feely, R.A., Weiss, R.F., Wanninkhof, R.H., Chipman, D.W., Sutherland, S.C., 1997. Global air-sea flux of CO₂: An estimate based on measurements of sea-air pCO₂ difference. *Proc. Natl. Acad. Sci.* 94, 8292–8299.

- Takahashi, T., Sutherland, S.C., Sweeney, C., Poisson, A., Metzl, N., Tilbrook, B., Bates, N., Wanninkhof, R., Feely, R.A., Sabine, C., Olafsson, J., Nojiri, Y., 2002. Global sea-air CO₂ flux based on climatological surface ocean pCO₂, and seasonal biological and temperature effects. *Deep. Res. Part II Top. Stud. Oceanogr.* 49, 1601–1622.
- Takahashi, T., Sutherland, S.C., Wanninkhof, R., Sweeney, C., Feely, R.A., Chipman, D.W., Hales, B., Friederich, G., Chavez, F., Sabine, C., Watson, A., Bakker, D.C.E., Schuster, U., Metzl, N., Yoshikawa-Inoue, H., Ishii, M., Midorikawa, T., Nojiri, Y., Körtzinger, A., Steinhoff, T., Hoppema, M., Olafsson, J., Arnarson, T.S., Tilbrook, B., Johannessen, T., Olsen, A., Bellerby, R., Wong, C.S., Delille, B., Bates, N.R., de Baar, H.J.W., 2009. Climatological mean and decadal change in surface ocean pCO₂, and net sea-air CO₂ flux over the global oceans. *Deep. Res. Part II Top. Stud. Oceanogr.* 56, 554–577.
- Upstill-Goddard, Robert C, 2006. Air-sea gas exchange in the coastal zone. *Estuar. Coast. Shelf Sci.* 70, 388–404.
- USGS Water Resources, 2019a. USGS 08211500 Nueces Rv at Calallen, TX.
- USGS Water Resources, 2019b. USGS 08211000 Nueces Rv nr Mathis, TX
- Vachon, D., Prairie, Y.T., Cole, J.J., 2010. The relationship between near-surface turbulence and gas transfer velocity in freshwater systems and its implications for floating chamber measurements of gas exchange. *Limnol. Oceanogr.* 55, 1723–1732.
- van der Werf, G.R., Morton, D.C., DeFries, R.S., Olivier, J.G.J., Kasibhatla, P.S., Jackson, R.B., Collatz, G.J., Randerson, J.T., 2009. CO₂ emissions from forest loss. *Nat. Geosci.* 2, 737–738.
- Wanninkhof, R., 2014. Relationship between wind speed and gas exchange over the ocean revisited. *Limnol. Oceanogr. Methods* 12, 351–362.

- Wanninkhof, R., Asher, W.E., Ho, D.T., Sweeney, C., McGillis, W.R., 2009. Advances in Quantifying Air-Sea Gas Exchange and Environmental Forcing. *Ann. Rev. Mar. Sci.* 1, 213–244.
- Wanninkhof, R., McGillis, W.R., 1999. A cubic relationship between air-sea CO₂ exchange and wind speed. *Geophys. Res. Lett.* 26, 1889–1892.
- Wanninkhof, R.H., 1992. Relationship between wind speed and gas exchange. *J. Geophys. Res.* 97, 7373–7382.
- Weiss, R.F., 1974. Carbon dioxide in water and seawater: the solubility of a non-ideal gas. *Mar. Chem.* 2, 203/2015.
- Weiss, R.F., Price, B.A., 1980. Nitrous oxide solubility in water and seawater. *Mar. Chem.* 8, 347–359.
- Wollast, R., 1998. Evaluation and comparison of the global carbon cycle in the coastal zone and in the open ocean, in: Brink, K.H., Robinson, A. r. (Eds.), *The Global Coastal Ocean*. John Wiley & Sons, New York, pp. 213–252.
- Woolf, D.K., 1993. Bubbles and the air-sea transfer velocity of gases. *Atmos. - Ocean* 31, 517–540.
- Yao, H., Hu, X., 2017. Responses of carbonate system and CO₂ flux to extended drought and intense flooding in a semiarid subtropical estuary. *Limnol. Oceanogr.* 62, S112–S130.
- Zappa, C., Asher, W.E., Jessup, A.T., 2001. Microscale wave breaking and air-water gas transfer. *J. Geophys. Res.* 106, 9385–9391.
- Zappa, C.J., Raymond, P.A., Terray, E.A., McGillis, W.R., 2003. Variation in surface turbulence and the gas transfer velocity over a tidal cycle in a macro-tidal estuary. *Estuaries and Coasts* 26, 1401–1415.

Zeebe, R.E., Ridgwell, A., Zachos, J.C., 2016. Anthropogenic carbon release rate unprecedented during the past 66 million years. *Nat. Geosci.* 9, 325–329.

Zeebe, R.E., Wolf-Gladrow, D., 2001. *CO₂ In Seawater: Equilibrium, Kinetics, Isotopes*, 2nd ed. Elsevier Science B.V., Amsterdam.

LIST OF APPENDICES

APPENDICES	PAGE
Appendix A	56

Appendix A

The following set of sample calculations are for real data measured between 9:30 AM and 10:30 AM on 12/01/2018.

Raw Data:

Table A. 1 Sample data set from eddy covariance equipment.

Time Stamp (UTC)	Flux ($\mu\text{mol m}^{-2} \text{s}^{-1}$)	Atmospheric $x\text{CO}_2$ (ppm)	Air Temperature ($^{\circ}\text{C}$)	Relative Humidity (%)	U Velocity (m s^{-1})	V Velocity (m s^{-1})
12/1/2018 9:30	0.05	392.7	21.5	91.1	3.65	3.24
12/1/2018 9:45	0.36	392.8	21.5	90.9	3.55	3.00
12/1/2018 10:00	0.46	393.3	21.5	90.9	3.15	2.63
12/1/2018 10:15	3.33	394.8	21.3	90.9	4.17	-2.18
12/1/2018 10:30	1.43	395.6	20.7	91.6	4.54	-2.90

Table A. 2 Sample data set from SAMI- CO_2 sensor.

Time Stamp (UTC)	Sea Surface $x\text{CO}_2$ (ppm)	Sea Temperature ($^{\circ}\text{C}$)
12/1/2018 9:30	298	16.32
12/1/2018 10:00	308.7	16.51
12/1/2018 10:30	310	16.74

Step 1 – bin-average readings to hourly periods to mitigate against outliers. The averaged measurements were reported to the hour and were taken as an average of the all readings taken within 30 minutes of the hour. The average flux example is shown below:

$$\bar{F} = \frac{0.50 + 0.357 + 0.461 + 3.33 + 1.43}{5}$$

The SAMI-CO2 data was treated in a similar fashion but as the average of three readings instead of five. The final values for both data sets are shown in Table A.2.

Table A. 3 Hourly-averaged sample data for eddy covairance data

Time Stamp (UTC)	Flux ($\mu\text{mol m}^{-2}\text{s}^{-1}$)	Atmospheric $x\text{CO}_2$ (ppm)	Air Temperature ($^{\circ}\text{C}$)	Relative Humidity (%)	U Velocity (m s^{-1})	V Velocity (m s^{-1})	Sea Surface $x\text{CO}_2$ (ppm)	Sea Temperature ($^{\circ}\text{C}$)
12/1/20 18 10:00	1.126	393.8	21.29	91.07	3.811	0.7569	305.9	16.52

Step 2 – calculate velocity from individual vector components, where

$$U = \sqrt{U_{vel}^2 + V_{vel}^2}$$

$$U = \sqrt{3.811^2 + 0.7569^2} = 3.885 \text{ m s}^{-1}$$

Step 3 – calculate wind speed at a height of 10 m above sea surface using Equation 10 (Hsu et al., 1994).

$$U_{10} = 3.885 * \left(\frac{10}{3}\right)^{0.11} = 4.435$$

Step 4 - calculate dry pCO_2 in atm from xCO_2 in ppm

$$pCO_2 = xCO_2(P - pH_2O * RH)$$

where pH_2O is the saturated water vapor pressure calculated using Weiss and Price (1980), with average sea temperature, T , of 289.67 K and salinity, S , of 21.4.

$$\ln(pH_2O) = 24.4543 - 67.4509 * (100/T) - 4.8489 * \ln(T/100) - 0.000544 * S$$

$$pH_2O = 0.0183$$

The calculated vapor pressure is in atmospheres. To calculate the dry-partial pressure of CO_2 , with barometric pressure (0.9908 atm) taken from the weather station and $RH = 91.07\%$.

$$(pCO_2)_{dry,atm} = 393.8 \times 10^{-6} * (0.9908 - 0.9107 * 0.0183) = 3.863 \times 10^{-4} \text{ atm}$$

Step 5 – calculate K_0 (moles $L^{-1} \text{ atm}^{-1}$) with absolute water temperature ($T = 289.67 \text{ K}$) and salinity ($S = 21.4$) (Weiss, 1974).

$$K_0 = \exp[a + b(100/T) + c \times \ln(T/100) + S * (d + e(T/100) + f(T/100)^2)]$$

where

a	-58.0931
b	90.5069
c	22.294
d	0.027766
e	-0.025888
f	0.0050578

For the sample data, this gives a K_0 value of 0.0392 moles ($L^{-1} atm^{-1}$).

Step 6 - calculate k correcting for discrepancies in units, to give k in cm/hr.

$$k = \frac{F}{K_0 * \Delta pCO_2} \times \frac{1 \text{ mol}}{10^6 \mu\text{mol}} \times \frac{1 \text{ m}^3}{1000 \text{ L}} \times \frac{100 \text{ cm}}{\text{m}} \times \frac{3600 \text{ s}}{\text{hr}}$$

For the sample data, this gives k of 124.4 $cm \text{ hr}^{-1}$

Step 7 – calculate Schmidt number using data from Wanninkhof (2014), with temperature (t) in °C, data gives Sc numbers at salinity = 35 and salinity = 0, Sc at $S = 21.4$ obtained from linear interpolation.

$$Sc = a + bt + ct^2 + dt^3 + et^4$$

where

	S = 0	S = 35
a	1923.6	2116.8
b	-125.06	-136.25
c	4.3773	4.7353
d	-0.08568	-0.092307
e	0.000703	0.0007555

For the sample data, this gives a Sc of 777.9

Step 8 – Normalize k to a Schmidt number of 660 using Equation 8 (Liss and Merlivat, 1986).

$$k_x = k_{660} * \left(\frac{Sc}{660} \right)^n$$

U_{10} for the sample data is 3.885 $m \text{ s}^{-1}$, so value of n in Equation 8 is -0.5. This gives a value for k_{660} of 114.3 $cm \text{ hr}^{-1}$. for the sample data.